Acta Geochim (2019) 38(4):587–609
https://doi.org/10.1007/s11631-019-00355-9

ORIGINAL ARTICLE

Geological and geochemical characteristics of the Baogudi Carlin-type gold district (Southwest Guizhou, China) and their geological implications

Songtao Li[1,2,3] · Yong Xia[1] · Jianzhong Liu[4] · Zhuojun Xie[1] · Qinping Tan[1] · Yimeng Zhao[1,2] · Minghua Meng[3] · Lijin Tan[3] · Rong Nie[3] · Zepeng Wang[3] · Guanghong Zhou[5] · Haiyan Guo[6]

Received: 23 January 2019 / Revised: 3 May 2019 / Accepted: 29 May 2019 / Published online: 14 June 2019

Abstract The newly discovered Baogudi gold district is located in the southwestern Guizhou Province, China, where there are numerous Carlin-type gold deposits. To better understand the geological and geochemical characteristics of the Baogudi gold district, we carried out petrographic observations, elemental analyses, and fluid inclusion and isotopic composition studies. We also compared the results with those of typical Carlin-type gold deposits in southwestern Guizhou. Three mineralization stages, namely, the sedimentation diagenesis, hydrothermal (main-ore and late-ore substages), and supergene stages, were identified based on field and petrographic observations. The main-ore and late-ore stages correspond to Au and Sb mineralization, respectively, which are similar to typical Carlin-type mineralization. The mass transfer associated with alteration and mineralization shows that a significant amount of Au, As, Sb, Hg, Tl, Mo, and S were added to mineralized rocks during the main-ore stage. Remarkably, arsenic, Sb, and S were added to the mineralized rocks during the late-ore stage. Element migration indicates that the sulfidation process was responsible for ore formation. Four types of fluid inclusions were identified in ore-related quartz and fluorite. The main-ore stage fluids are characterized by an H_2O–NaCl–CO_2–CH_4 ± N_2 system, with medium to low temperatures (180–260 °C) and low salinity (0–9.08% NaCl equivalent). The late-ore stage fluids featured H_2O–NaCl ± CO_2 ± CH_4, with low temperature (120–200 °C) and low salinity (0–7.48% NaCl equivalent). The temperature, salinity, and CO_2 and CH_4 concentrations of ore-forming fluids decreased from the main-ore stage to the late-ore stage. The calculated $\delta^{13}C$, δD, and $\delta^{18}O$ values of the ore-forming fluids range from − 14.3 to − 7.0‰, −76 to −55.7‰, and 4.5–15.0‰, respectively. Late-ore-stage stibnite had $\delta^{34}S$ values ranging from − 0.6 to 1.9‰. These stable isotopic compositions indicate that the ore-forming fluids originated mainly from deep magmatic hydrothermal fluids, with minor contributions from strata. Collectively, the Baogudi metallogenic district has geological and geochemical characteristics that are typical of Carlin-type gold deposits in southwest Guizhou. It is likely that the Baogudi gold district, together with other Carlin-type gold deposits in southwestern Guizhou, was formed in response to a single widespread metallogenic event.

Keywords Elemental geochemistry · Fluid inclusions · Stable isotopes · Carlin-type gold deposits · Baogudi gold district · Southwestern Guizhou

Electronic supplementary material The online version of this article (https://doi.org/10.1007/s11631-019-00355-9) contains supplementary material, which is available to authorized users.

✉ Yong Xia
xiayong@vip.gyig.ac.cn

1 State Key Laboratory of Ore Deposit Geochemistry, Institute of Geochemistry, Chinese Academy of Sciences, Guiyang 550081, China

2 University of Chinese Academy of Sciences, Beijing 100049, China

3 No. 105 Geological Team, Guizhou Bureau of Geology and Mineral Exploration and Development, Guiyang 550018, China

4 Bureau of Geology and Mineral Exploration and Development Guizhou Province, Guiyang 550004, China

5 Guizhou Education University, Guiyang 550018, China

6 School of Pharmacy, Chengdu University of Traditional Chinese Medicine, Chengdu 611137, China

1 Introduction

The Yunnan-Guizhou-Guangxi "golden triangle" in southwestern China is the second-largest Carlin-type gold mineralized region in the world, ranking after the largest in Nevada, USA (Su et al. 2018). More than 200 Carlin-type gold deposits and occurrences have been identified in the "golden triangle", with a total proven gold reserve of over 800 tonnes (Hu et al. 2017; Su et al. 2018), and the majority of these deposits are situated in the southwestern Guizhou Province (Xie et al. 2018). The most important Carlin-type gold deposits in southwest Guizhou include the Shuiyindong, Zimudang, Getang, Xiongwu, Nibao, and Jiadi deposits hosted in the platform-face strata and the Lannigou, Banqi, and Yata deposits hosted in the basin-facial strata. The Baogudi district is located in the platform-facial region and surrounded by the gold deposits mentioned above. In this district, a small gold deposit (the Dayakou gold deposit, 2.8 tonnes gold) was discovered during the early 20th century. Recent geological-geophysical-geochemical comprehensive investigations have indicated great potential for Carlin-type gold prospecting in the Baogudi district (Tan et al. 2017a). The area exhibits some geological characteristics of typical Guizhou Carlin-type gold deposits, such as host rocks, ore-controlling structures, ore body geometry, and alterations.

Although many investigations have been carried out on the Guizhou Carlin-type gold deposits, issues related to the fluid source, precipitation mechanisms, and genetic model remain unresolved and greatly debated. For example, Su et al. (2009) favored a metamorphic origin of the mineralizing fluids related to crustal thickening and prograde metamorphism and summarized that sulfidation and decarbonation were the principal mechanisms of gold precipitation. Additionally, Peng et al. (2014) concluded that metals were sourced from pre-enriched sediments by the circulation of meteoric water and that fluid immiscibility caused the precipitation and enrichment of gold. Most recently, Tan et al. (2015a, b) and Xie et al. (2018) proposed that a significant proportion of magmatic fluid was added to the ore fluid and contributed to the formation of the gold ore.

The Baogudi gold district belongs to the central part of the gold ore-centralization area in southwest Guizhou. As the main spatial connection for peripheral Carlin-type gold deposits, the Baogudi gold district plays a key role in transferring hydrothermal fluids and migrating metallogenic elements. Thus, the fluid inclusions, isotopic compositions, and bulk chemical compositions of this district can provide insight into the migration of ore-forming elements, as well as into the origin and evolution of the ore-forming fluids. Recent exploration led to the discovery of several ore bodies, which provided an excellent opportunity to investigate the geological-geochemical characteristics of gold mineralization in this district.

In this paper, we present detailed studies on the petrographic characteristics, element migration fluxes associated with mineralization, ore-forming fluid features, and C, H, O, and S isotopic compositions of the Baogudi gold deposit and compare them with those of typical Carlin-type gold deposits in southwest Guizhou, aiming to provide constraints for ore genesis in the Baogudi district and expand the understanding of the Carlin-type gold metallogenic system in southwest Guizhou.

2 Geological characteristics of Carlin-type gold deposits in southwest Guizhou

The Carlin-type gold deposits in southwestern Guizhou Province are tectonically located at the combinative region of the Yangtze craton and the Youjiang basin (Fig. 1) (Hu et al. 2002). These deposits mainly occur in the Upper Permian to Lower Triassic sedimentary strata. Mineralization is controlled by structure and lithology together. The Guizhou Carlin-type gold deposits are divided into two types based on their orebody occurrence, including strata-bound and fault-controlled mineralizations (Xia 2005). Strata-bound mineralization is controlled by anticlines or domes, such as in the Shuiyindong, Jiadi, and Getang deposits (Hu et al. 2018a, b; Tan et al. 2017a, b). Strata-bound orebodies are commonly hosted in permeable bioclastic limestone, basaltic rocks, or unconformities. Fault-controlled mineralization commonly occurs along high-angle reverse faults, with orebodies hosted in calcareous siltstones or basaltic pyroclastic rock, such as in the Jinfeng, Yata, and Nibao deposits (Liu et al. 2015; Wei et al. 2016).

The Carlin-type gold deposits in southwestern Guizhou share many similarities, including alteration, element associations, ore minerals, ore-forming fluids, and stable isotope compositions. (1) Alteration processes associated with gold precipitation include decarbonization to remove carbonate minerals (e.g., dolomite and calcite) from the rock, silicification in the form of jasperoid and vein quartz, and sulfidation with the formation of gold-bearing arsenian pyrite and minor arsenopyrite (Cline et al. 2013; Su et al. 2012; Tan et al. 2015a). (2) Signature ore elements include Au, As, Hg, Sb, and Tl, with low concentrations of base metals and barium (Hu et al. 2002; Tan et al. 2015a), and these elements are incorporated into arsenic-rich sulfides (e.g., arsenian pyrite, arsenopyrite, stibnite, realgar, and orpiment) (Su et al. 2008, 2012; Xie et al. 2017; Yan et al. 2018). Elemental paragenesis and differentiation are revealed by the ore chemical

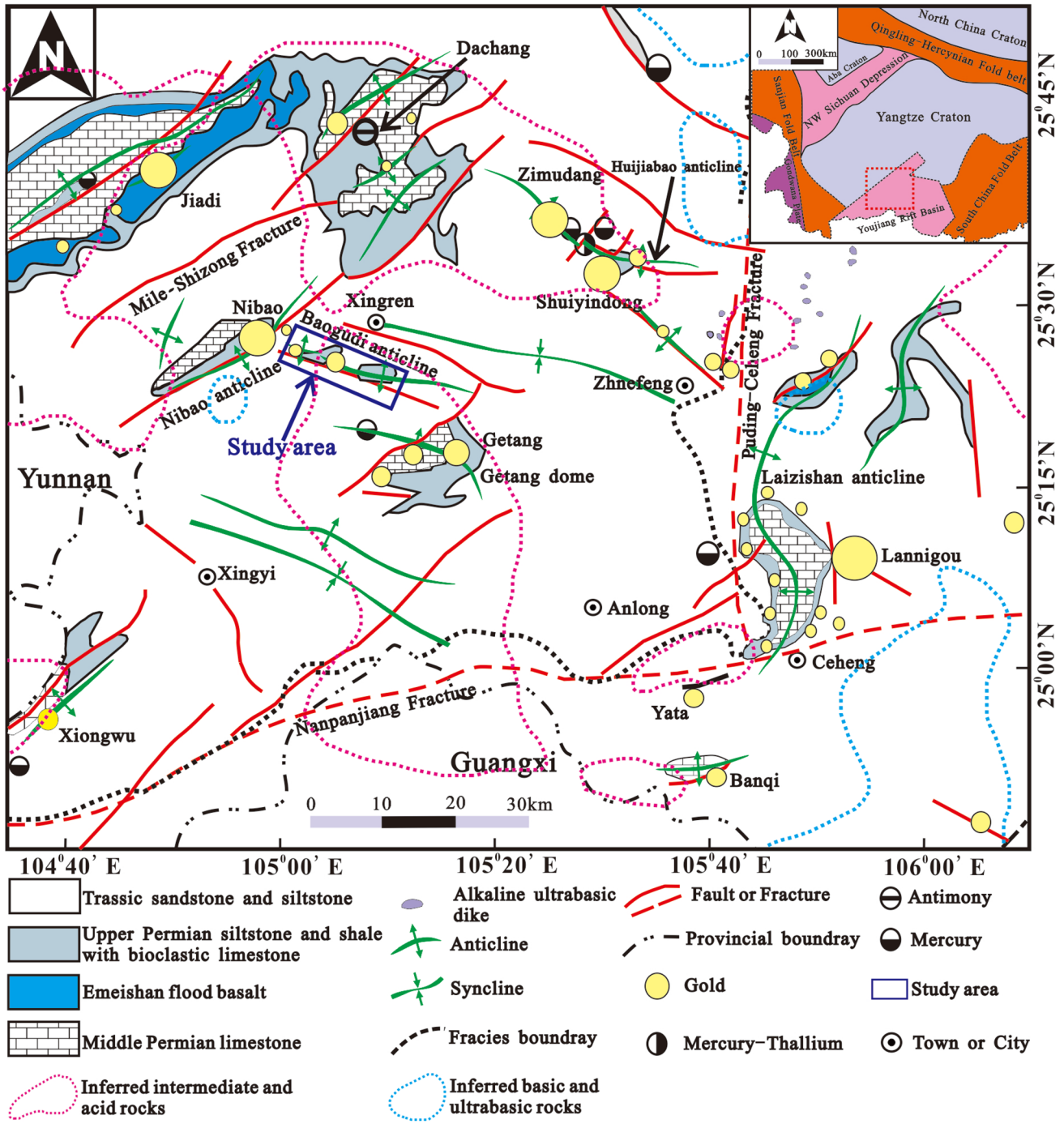

Fig. 1 Regional geological sketch map of southwestern Guizhou (modified after Su et al. 2009; Liu et al. 2017), showing the distribution of major Carlin-type gold, antimony, and mercury deposits and the projection boundary of pluton inferred by gravity and magnetic investigations

compositions of various deposits, such as the Shuiyindong gold deposit, Dachang antimony deposit, and Lan muchang mercury deposit (Hu et al. 2002). (3) These deposits generally formed at depths between 1.5 and 4.3 km, pressures of 0.5–2.3 kbar, and temperatures of ~ 190 to 300 °C from low-salinity (1.6–3.3% NaCl equivalent) and CO_2-rich (6.3–8.4 mol%) reduced fluids (Gu et al. 2012; Su et al. 2009; Zhang et al. 2003). (4) The hydrogen and oxygen isotope values of quartz and clay minerals from several Guizhou Carlin-type gold deposits are relatively dispersed, and almost all data plot below the field of metamorphic fluids, with many in the field of formation fluids, as well as close to the meteoric water line (Hofstra et al. 2005; Peng et al. 2014; Tan et al. 2015b). Calcites

formed during the ore stage have negative $\delta^{13}C$ values, ranging from − 3 to − 9‰, which differs from those of diagenetic calcites with positive $\delta^{13}C$ values (Tan et al. 2015b; Wang et al. 2013). The $\delta^{34}S$ value of ore pyrite, arsenopyrite, realgar, orpiment, and stibnite typically ranges from − 5 to 5‰ (Hu et al. 2018b; Xie et al. 2018; Hou et al. 2016; Tan et al. 2015b; Wang et al. 2013).

3 Geology of the Baogudi gold district

The Baogudi metallogenic area lies ~ 20 km south of the County of Xingren in southwestern Guizhou, China. The structural deformation is relatively intense in this study area, resulting in the formation of a complex fault-fold structural belt which comprises Baogudi anticlinorium and several groups of oblique faults (Figs. 2a, 3). The Baogudi anticlinorium, which is approximately 28 km long and 5 km wide, includes the Dayakou, Goupiqing and Magudi anticlines and the Goutou syncline. These secondary folds extend from east to west, with limbs dipping 10°–45°. The limbs adjacent to the core of the anticline are cut by a series of reverse faults oriented subparallel to the axis (Fig. 3). This is similar to the structural model (reverse faults in domes or anticlinal structures) of typical gold deposits in southwest Guizhou (Kuang et al. 2012). The oblique fault system is dominated by the nearly east–west-trending high-angle reverse faults, which mainly include the Goupiqing fault (F_5), Sifangqiu fault (F_7), Dayakou fault (F_9), and Maanshan fault (F_{11}). In some places, this set of reverse faults is disturbed by younger north-east- and north-west-trending faults. The main ore-controlling structures within the field are the east–west-trending anticlines and axial reverse faults.

The exposed stratum in the Baogudi metallogenic area includes the Permian Maokou, Longtan, Changxing, and Dalong Formations, the Triassic Feixianguan and Yongningzhen Formations, and minor Quaternary sediment (Fig. 2a, b). The massive bioclastic limestone of the Permian Maokou Formation (P_2m) is generally exposed in the core of the anticline around the Anzhe district. An unconformity (referred to as SBT) is widely developed between the Maokou and Longtan Formations. The SBT, interpreted as being formed jointly by sedimentation, regional tectonic action, and hydrothermal alteration (Liu et al. 2009; Xia 2005), generally consists of silicalite, strongly silicified brecciated limestone, and clasolite. Controlled-source audio-frequency magnetotelluric (CSAMT) indicate that the contact above the Maokou Formation is usually buried at a depth of less than 1000 m (Fig. 3). The Longtan Formation (P_3l), which is mainly exposed in the core of the Baogudi anticlinorium, is subdivided into two units according to the lithological characteristics. The first unit (P_3l^1) is dominated by limestone, while the second unit (P_3l^2) contains predominately clasolite. Organic carbon is common in this formation. The Changxing-Dalong Formation ($P_3c + d$) is comprised of argillite and siltstone intercalated with bioclastic limestone. Triassic strata in the district are composed of fine clasolite and carbonate rocks. Gold mineralization is localized preferentially in the bioclastic limestone and calcareous siltstone of the Longtan Formation, with some ore bodies occurring in the strongly silicified brecciated limestone and clasolite of the SBT.

Basalt is distributed approximately 10 km east of the Baogudi metallogenic area. No felsic intrusive rocks have been discovered in the Baogudi area. However, gravity and magnetic data indicate that extensive intermediate-acid intrusive bodies are concealed in the southwest Guizhou, including in the study area, and are buried at depths of 2–5 km (Liu et al. 2017; Wang et al. 2009, 2015). Furthermore, the anomaly distribution of Carlin-type elements and the locations of gold deposits coincide with the geophysical anomalies of buried intermediate-acid intrusions, demonstrating that gold mineralization is spatially associated with the magmatism (Wang et al. 2015).

In addition to the Dayakou gold deposit, there are five recently discovered gold occurrences (i.e., Jiaozishan, Shuijingwan, Goutou, Anzhe, and Houzipo) in the Baogudi metallogenic area (Fig. 2a). Notably, these gold deposits or occurrences occur as ore trends in keeping with the east–west structure. To date, more than fifteen gold orebodies containing significant potential with total estimated resources of fifteen tons (average gold grade of 1.96 g/t) have been discovered. According to the orebody geometry, these newly discovered gold orebodies can be divided into two types, fault-controlled and strata-bound orebodies. The fault-controlled orebodies occur as vein or lenses within thrust fault zones along the anticlinal axis. They commonly occur at a dip parallel to the fault and strike east–west. These orebodies extend discontinuously to 440–1160 m long and have widths of 0.9–4.4 m. The strata-bound orebodies occur as stratiform, stratoid, and lenticular shapes and are hosted in interlayer fracture zones near the anticlinal culmination and unconformity (SBT) between the Maokou and Longtan Formations. These orebodies are typically 640–1200 m in length, 0.3–9.3 m in width and thin out gradually away from the anticline axis. The attitude of the orebodies is basically consistent with their country rocks.

The wall-rock alteration types observed in the Baogudi gold district include silicification (Figs. 4a–g, 5d–i, k–l), sulfidation (Figs. 4e–g, 5a–k), calcification (Fig. 4d), fluoritization (Figs. 4e, g, 5l), dolomitization (Fig. 5a, f–h), and decarbonation (Fig. 5g). These alterations, to be described in detail below, are similar to those of typical

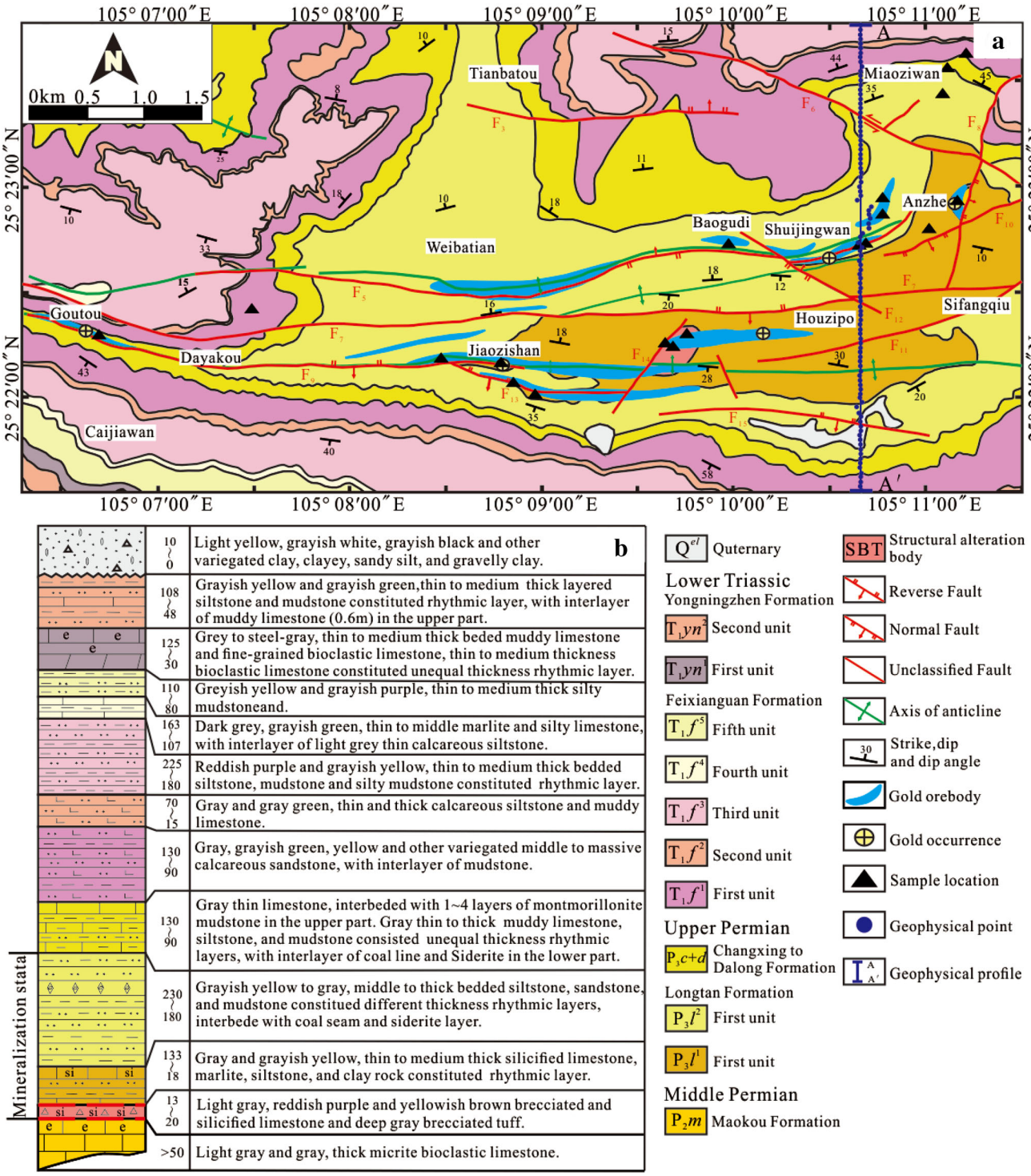

Fig. 2 Geological map (**a**) and stratigraphic column (**b**) of the Baogudi gold district

Carlin-type gold deposits in southwest Guizhou (Hu et al. 2002; Xia 2005). The results of geochemical exploration indicate that the Au, As, Sb, and Hg anomalies are closely related to all of these types of alteration. Particularly, Au anomalies mainly associate with the pyritized and silicified rock of P_3l, while Sb anomalies in the studied area are generally confined to the silicified rock of the SBT.

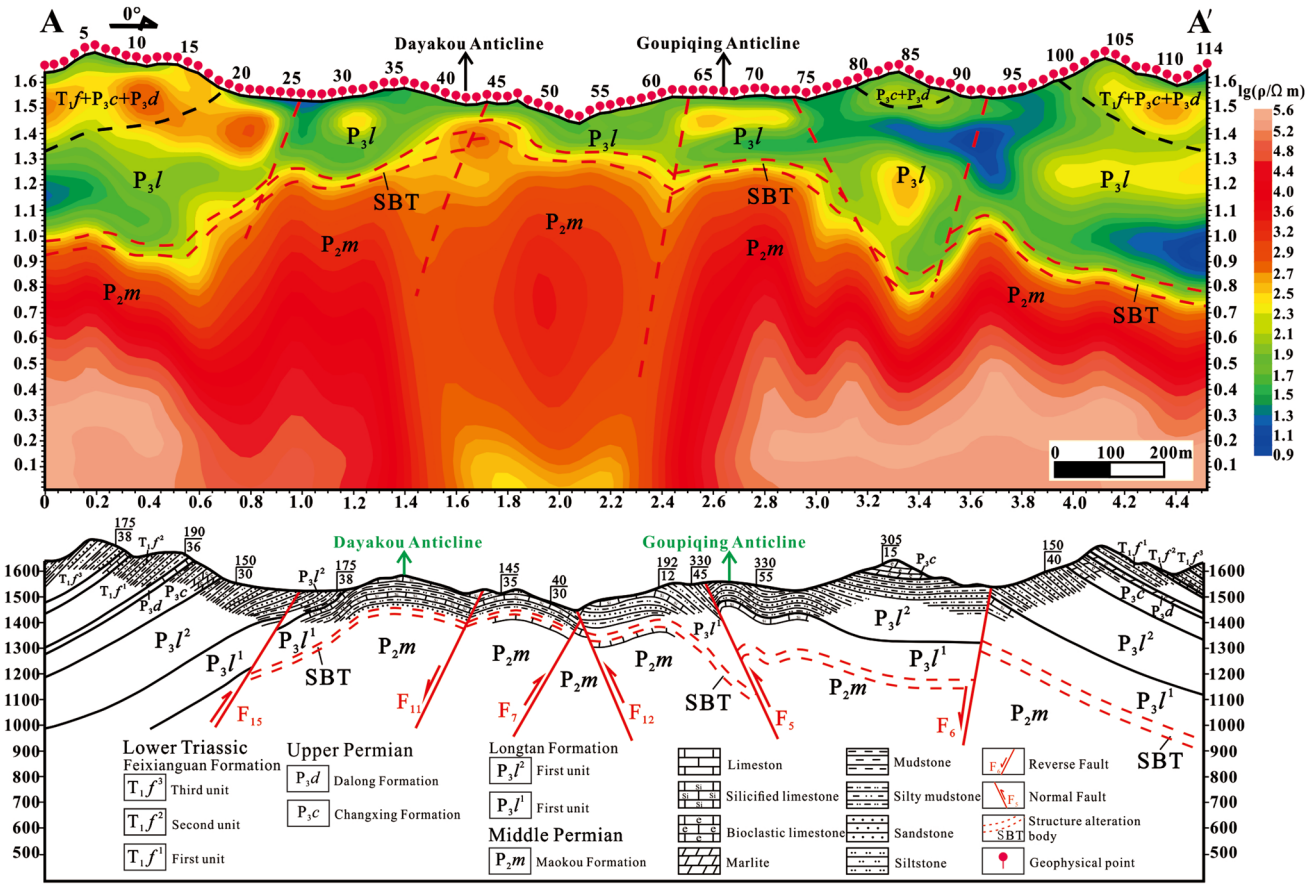

Fig. 3 Resistivity model of the nonlinear conjugate gradients algorithm for the controlled-source audio-frequency magnetotelluric 2D inversion and the corresponding geological profile from A–A′

4 Mineralization stage and paragenesis

Based on field and petrographic relationships, the mineralization paragenesis of the Baogudi gold district can be divided into three main stages: the sedimentation diagenesis stage, the hydrothermal stage (main-ore substage and late-ore substage), and the supergene stage. The mineral assemblage of each stage is summarized in Fig. 6

Sedimentationdiagenesisstage (*quartz* + *pyrite*).

This stage is represented by abundant pyrite, detrital quartz, ferroan dolomite, calcite, and clay minerals. Three types of pyrite were recognized according to texture, including framboidal pyrite, bioclastic pyrite, and coarse-grained euhedral pyrite. Framboidal pyrite is characterized by round to oval aggregates of 10–30 μm in diameter, and each framboid is comprised of numerous small hexagonal pyrite grains (less than 10 μm) (Fig. 5a). Bioclastic pyrite is commonly present as curved aggregates of several anhedral to subhedral grains (Fig. 5b). It retains the morphological characteristics of biogenetic texture and is generally less than 500 μm in length and 50 μm in width. Coarse-grained euhedral pyrite is randomly disseminated in the host rocks (Fig. 5c, d). The sections of coarse-grained pyrite commonly appear as a quadrangle, pentagon, and hexagon shapes with sizes ranging from 10 to 50 μm (Fig. 5d).

Detrital quartz (Fig. 5c, d), ferroan dolomite (Fig. 5a, f, g, h), calcite (Fig. 5d), and clay minerals (e.g., chlorite and illite) (Fig. 5a, f) constitute the rock matrix, and these minerals formed during sedimentation and diagenesis

Main − *ore substage* (*quartz* + *arsenian pyrite* + *arsenopyrite*).

This stage is the main Au mineralization stage and contains abundant pyrite, arsenopyrite, quartz, and minor dolomite. The pyrite can be divided into two types, including fine-grained pyrite and zoned pyrite. Qualitative energy dispersive analysis (EDS) indicates that the fine-grained pyrite is enriched with As. Fine-grained pyrite occurs in the quartz vein crosscutting ore (Fig. 5e) or is distributed in the altered rock. Locally, small fractures of mineralized rock are filled by veined aggregates of fine-grained anhedral pyrite, coarse-grained pyrite, and minor sphalerite and rutile (Fig. 5f). Zoned pyrite is characterized by a core-rim texture and is commonly surrounded by

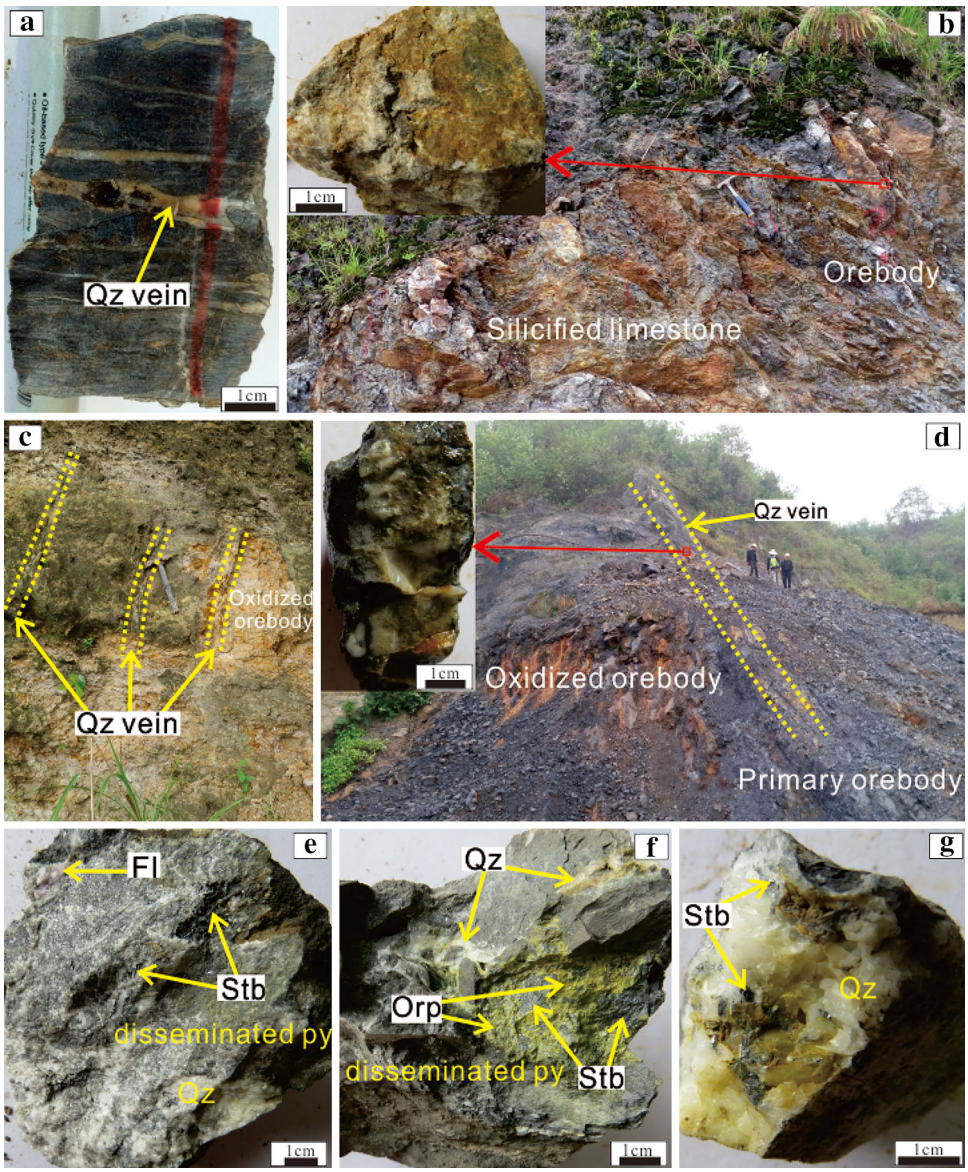

Fig. 4 Representative wall-rock alteration types in the Baogudi gold district. **a** Bedding-parallel banded quartz vein in silicified siltstone; **b** quartz stockwork in silicified limestone; **c** quartz vein vertically cutting the orebody; **d** quartz vein distributed in the orebody; **e** fluorite, quartz, and stibnite patches filling the open spaces of pyritized host rock; **f** orpiment occurring with quartz, stibnite, and disseminated pyrite; **g** vein quartz containing stibnite. *Qz* quartz, *Fl* fluorite, *Orp* orpiment, *Py* pyrite

quartz and dolomite. The zoned pyrite commonly contains an irregular margin with variations in thickness and inner core. The pyrite core commonly has a "porous" appearance (Fig. 5g), probably due to the inversion of marcasite into pyrite (Murowchick and Barnes 1986). Occasionally, this pyrite consists of three parts, including a core of anhedral or subhedral pyrite, an inner rim of As-rich pyrite, and an outer rim of As-poor pyrite (Fig. 5g).

Arsenopyrite is typically present as idiomorphic acicular, rhombohedral, columnar, and spear-shaped grains ranging in size from 1 to 100 μm. Commonly, arsenopyrite occurs in aggregates (Fig. 5h–i) with several grains or in isolation (Fig. 5i). Arsenopyrite rims pyrite and partially corrodes it, indicating that pyrite formed earlier than arsenopyrite. Liu (2003) and Su et al. (2008) documented that gold is predominantly present in arsenian pyrite, with lesser amounts in arsenopyrite.

Quartz occurs as veins and jasperoid. A large amount of cross-cutting—rather than layer-parallel—quartz veins and veinlets characterized by texture are indicative of open space filling (Figs. 4a, c, d, 5e). In contrast, jasperoid quartz formed by replacing carbonate minerals (e.g., ferroan dolomite) generally contains significant encapsulated quantities of tiny dolomite and ferroan dolomite (Figs. 4b, 5g, h). This jasperoid quartz typically has variable grain sizes and xenomorphic textures (Fig. 5f–h). Dolomite (Fig. 5g), which is absent from low-grade samples, is intergrown with ferroan dolomite in the ore

$$Late-ore\ substage(quartz+stibnite+fluorite \pm orpiment \pm realgar).$$

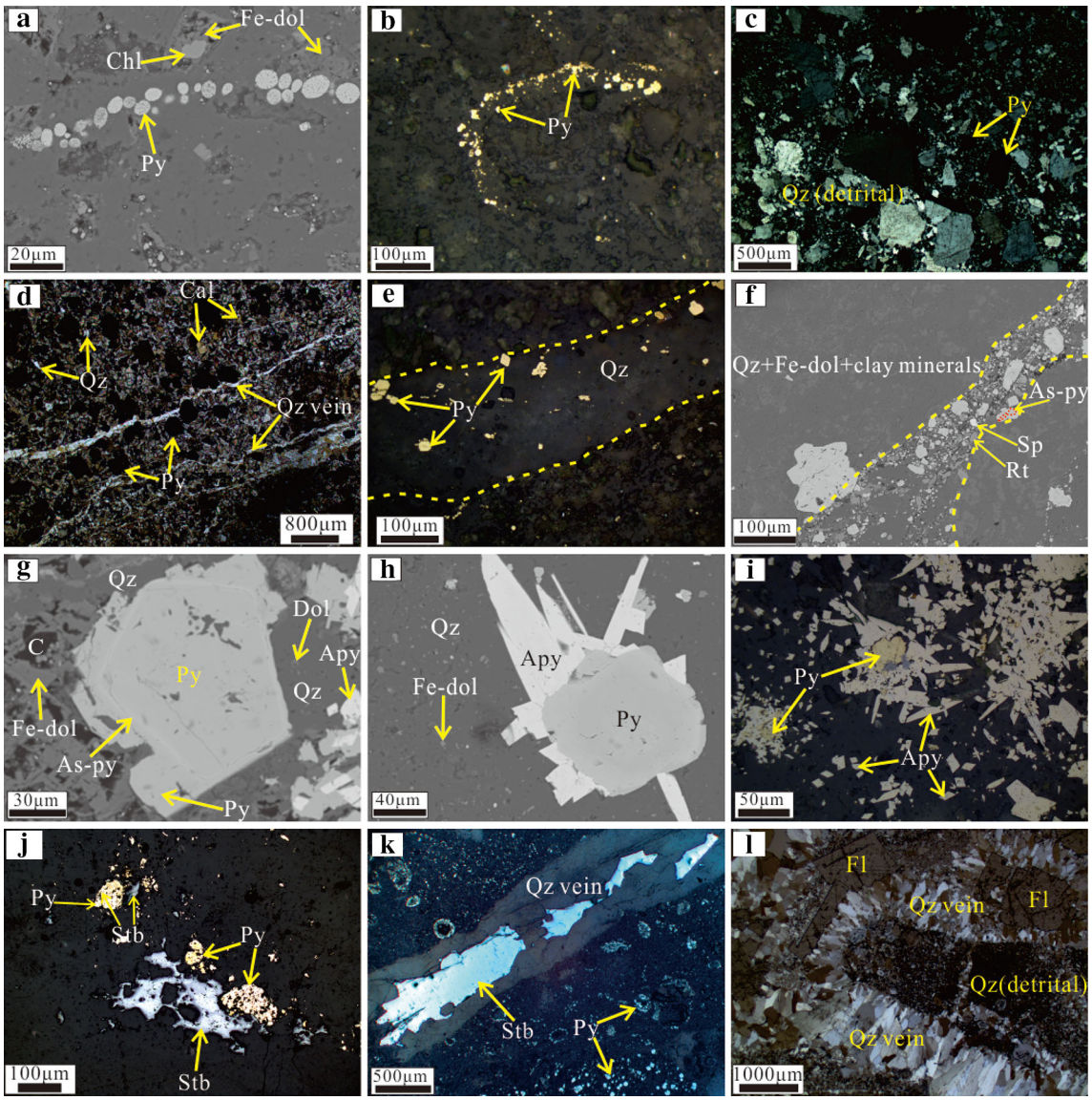

Fig. 5 Minerals and their relationships in the Baogudi gold district. **a** framboidal pyrite; **b** bioclastic pyrite; **c** coarse-grained euhedral-subhedral pyrite distributed in detrital quartz; **d** coarse-grained pyrite disseminated in a matrix of detrital quartz and calcite, which is cut by a late quartz vein; **e** quartz-pyrite vein crosscutting the host rock; **f** pyrite-rutile-sphalerite vein crosscutting the host rock; **g** jasperoidal quartz, Fe-dolomite, and dolomite occurring with zoned pyrite and arsenopyrite; **h** arsenopyrite overgrowing pyrite; **i** coexistence of arsenopyrite and pyrite; **j** pyrite containing inclusions of stibnite or encompassed by embayed-texture stibnite; **k** stibnite distributed in a quartz vein; **l** fragments of the host rock and fluorite grains cemented by drusy quartz. **a**, **f**, **g**, **h** Backscattered electron (BSE) images, **b**, **e**, **i**, **j**, **k** are taken under transmitted light and **c**, **d**, **l** are taken under transmitted light. *Py* pyrite, *As-Py* arsenian pyrite, *Apy* arsenopyrite, *Stb* stibnite, *Sp* Sphalerite, *Rt* Rutile, *Qz* quartz, *Dol* dolomite, *Fe-dol* Fe-dolomite, *Chl* Chlorite, *Fl* fluorite

This stage is dominated by assemblages of stibnite, fluorite, quartz, and minor-trace orpiment and realgar. A distinctive feature of this stage is the widespread occurrence of stibnite, which commonly coexists with fluorite and orpiment (Figs. 4e, f, 5i). Locally, stibnite occurs as solid inclusions or embayed-textured shapes encompassed by pyrite (Fig. 5j), indicating that the stibnite was formed slightly later than the pyrite. In some cases, stibnite is enclosed within quartz (Figs. 4g, 5k).

Veined quartz typically (Figs. 4e, f, g, 5k, i) precipitates in the open spaces of altered rock. In some places, quartz veins crosscut early subhedral pyrite. Jasperoid quartz occurs but is not pervasive. Fragments of siltstones and fluorite grains are cemented or corroded by euhedral drusy quartz crystals (Fig. 5l)

Supergene stage (*limonite* + *valentinite*).

Supergene Fe and Sb minerals, such as limonite and valentinite (Fig. 5b, d), typify the post-ore mineralization.

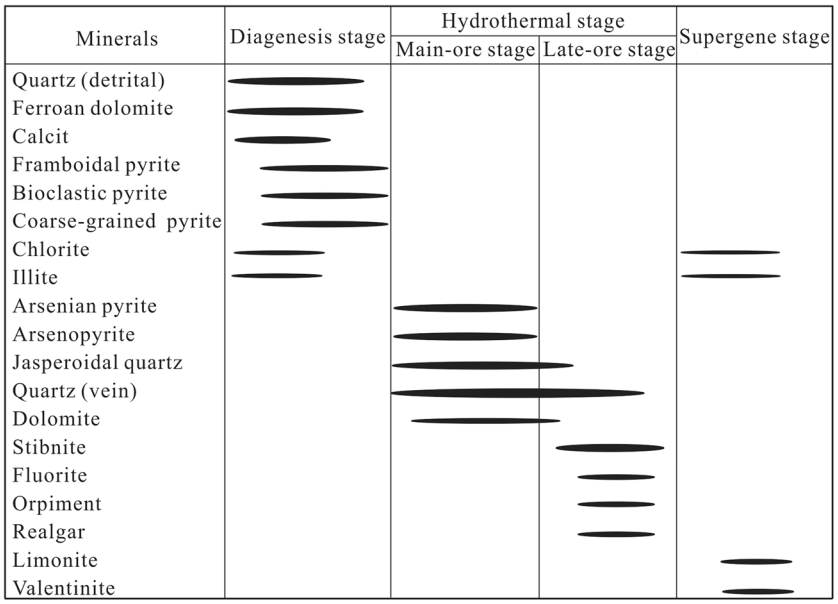

Fig. 6 Mineral paragenesis of the Baogudi gold district

This stage also contains clay minerals. These supergene minerals occur mainly near the surface, giving either soil or "pock-marked" (low-density porous) structures.

5 Sampling and analytical methods

5.1 Sampling

The samples for determining bulk chemical compositions, examining fluid inclusions, and performing C–H–O–S isotopic analysis were collected from field outcrops revealed by trenches and stopes. The sample locations are shown in Fig. 2a. Sixty-one polished thin sections were made for petrographic observation. Element geochemistry data were obtained from seventeen samples, including ore, altered rocks, and country rocks, and all these samples were located in the same horizon and lithology of P_3l^1 and the SBT. Twenty-six quartz and three fluorite samples were collected for fluid inclusion study and C–H–O isotopic analyses. Three stibnite samples from the SBT were analyzed for the S isotopic composition.

5.2 Analytical methods

5.2.1 Petrographic observation

Polished sections were prepared and examined using microscopy and scanning electron microscopy (SEM). Optical microscopy analysis using reflected and transmitted light were carried out to characterize the mineral composition and textural-structural features. An SM-7800F SEM at the State Key Laboratory of Ore Deposit Geochemistry, Institute of Geochemistry, Chinese Academy of Sciences (IGCAS) was used to provide semiquantitative chemical compositions to confirm minerals. Additionally, high-resolution images were collected using the SEM to identify paragenetic and textural relationships.

5.2.2 Elemental analysis

The analyses of major and trace elements were performed at the Guizhou Central Laboratory of Geology and Mineral Resources in Guiyang, China. Major elements were analyzed using a ZSX Primus IIX-ray fluorescence spectrometer (XRF) with an operating voltage of 50 kV, a current of 70 mA, and fused glass discs were used. The analytical precision was better than 5%.

The trace elements were analyzed using an X-Series II Inductively coupled plasma mass spectrometer (ICP-MS). Rhodium was used as an internal standard to monitor the signal drift during counting. This method provided data for Sb, Tl, Ba, Cr, Li, Ni, V, Zn, Sc, Be, Co, Cu, Ga, Ge, Rb, Sr, Mo, Cs, W, Pb, Th, U, Zr, Nb, Hf, Ta, Ag, Y, and fourteen rare earth elements. Gold was analyzed by the fire assay method. Mercury and As were analyzed by inductively coupled plasma atomic emission spectrometry (ICP-AES). The analytical precisions for all elements were better than 5%.

5.2.3 Fluid inclusion analysis

Based on fluid inclusion observations under a standard optical petrographic microscope, representative inclusions were selected for detailed microthermometric and laser Raman spectroscopic studies at the fluid inclusion laboratory, IGCAS.

Microthermometric measurements taken made on a Linkam THMSG 600 programmable heating-freezing stage mounted on a Leica microscope coupled to an image analysis system. The equipment was calibrated with synthetic fluid inclusions. The microthermometric data were measured at temperatures from − 196 to + 600 °C and have an uncertainty of about ± 0.2 below 50 °C and of ± 2 °C for temperatures above 100 °C. Temperatures were changed at 10 °C/min during the heating and freezing processes and at rates between 0.1 and 1 °C/min near the phase transition point. Volatile species in individual fluid inclusions that were representative of particular populations were analyzed using a Renishaw 2000 laser Raman microspetrometer (LRM). The source was an argon-ion laser with a wavelength of 514.5 nm and a laser power of 20 nw. The spot size of the laser beam was approximately 1 μm, with a spectral resolution of 2 cm^{-1}. The scanning times were 10, 30, and 60 s with the scanning range of 150–4500 cm^{-1}.

5.2.4 Stable isotope analyses

Samples for stable isotope analyses were crushed to 40–60 mesh, sieved and picked out using a binocular microscope. Hydrogen, C, O, and S isotopic compositions were analyzed at the Analytical Laboratory of the Research Institute of Uranium Geology in Beijing, China. The H, O, and C isotopic compositions of quartz were analyzed using the Finnigan MAT253-type mass spectrometer, and the S isotopic compositions of stibnite were analyzed using the Finnigan MAT251-type mass spectrometer. Oxygen was liberated for isotopic analyses using BrF_5 (Clayton and Mayeda 1963). Fluids released by crushing reacted with zinc to produce hydrogen at high temperatures (Coleman et al. 1982). Fluids were released from fluid inclusions by heating through four different temperature stages prior to carbon isotopic analysis and then reacted with Cu_2O to produce pure CO_2 (Liu et al. 2013). Stibnite was converted into SO_2 for S isotopic analyses by a quantitative oxidation reaction with Cu_2O at a temperature of 980 °C (Liu et al. 2013). The H, O, C, and S isotopic analysis results adopted the Standard Mean Ocean Water (SMOW), Pee Dee Belemnite (PDB), and Canyon Diablo Troilite (CDT) standards, respectively, with a precision of ± 2‰ for δD and of ± 0.2‰ for $\delta^{18}O$, $\delta^{13}C$, and $\delta^{34}S$, respectively.

6 Results

6.1 Mass transfer associated with alteration and mineralization

In the zone of the P_3l from the Baogudi gold district, the gold content of the mineralized siltstone ranges between 1.79 and 3.54 ppm. The concentrations of other Carlin-suite elements are consistently at a very high level. Similar geochemical features are also observed in the silicified limestone, in which the gold content varies from 0.87 to 1.86 ppm. In the zone of the P_3l^2, the contents of these elements (Au, As, Sb, Hg, and Tl) are similar to those in the zone of the P_3l^1. The unmineralized rock of the Longtan Formation has a lower gold content, while the contents of As, Hg, Sb, and Tl consistently decrease. In the zone of the intensely silicified limestone of the SBT, the assays did not reveal significant gold contents, with measured amounts ranging from 0.03 to 0.13 ppm. These modified rocks, however, are characterized by relatively high contents of As, Sb, and Tl. The antimony content was abnormally high at up to 3.5–12.29%. Such elevated contents of these elements are consistent with petrographic evidence and geochemical anomalies, according to which Sb anomalies are specifically associated with the antimony mineralization in silicified rock from the SBT.

Elemental fluxes during alteration and mineralization can be recognized by comparison of unaltered samples to their strongly mineralized or altered counterparts using immobility isocon diagrams (Grant 1986; Gresens 1967). Titanium and Al are generally considered to be immobile elements during the alteration and mineralization of Carlin-type gold deposits (Kesler et al. 2003; Yigit and Hofstra 2003). The highly significant R^2 value of 0.932 for the plot of TiO_2 versus Al_2O_3 (Fig. 7) further indicates the immobile behavior of the two elements. Additionally, Zr and Th have been demonstrated to be immobile elements (Finlow-Bates and Stumpfl 1981). The regression line of the immobile elements Al_2O_3, TiO_2, Zr, and Th in the X–Y concentration plots is the immobility isocon, and the slope of this line defines the mass change during the alteration. Elements that lie above the immobility isocon are added to the rock during mineralization and alteration, and those

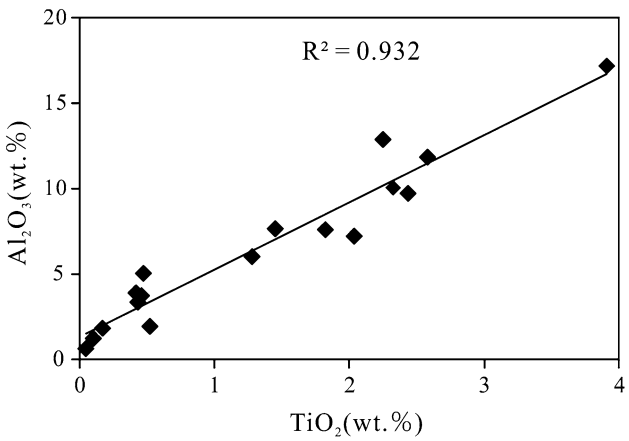

Fig. 7 Correlation plot showing the relation between Al_2O_3 and TiO_2

that lie below the immobility isocon are removed from the rock (Grant 1986; Gresens 1967).

Selected comparative samples were obtained from unaltered siltstone and mineralized counterparts (according to Au mineralization in the main-ore stage) of P_3l^1 and from unmineralized silicified limestone and mineralized counterparts (according to Sb mineralization in the late-ore stage) of the SBT. The immobility isocon plots in Fig. 8a show additions and losses of elements during alteration and mineralization in the main-ore stage. The ore and country rock samples were collected from the siltstone of the P_3l^1 (D05 and D21). The immobility isocon diagram shows that As, Au, Mo, Li, Sb, S, and Ag were added to the ore. In addition, Hg, Tl, Sc, Cu, Co, MgO, CaO, Ni, W, V, and Na_2O were added to the ore. P_2O_5 and Be were removed from the country rock. Fe_2O_3, SiO_2, and K_2O were immobile in the rock. The immobility isocon plot in Fig. 8b shows additions and losses of elements during alteration and mineralization in the late-ore stage. The mineralized rock and counterparts were collected from the limestone of the SBT (D11-2d and D18). The immobility isocon diagram shows that As, Sb, S, Ag, and Pb were significantly added to the altered rock. Tungsten, Li, Mo, MnO, and Sr were removed from the country rock. Gold, Hg, CaO, MgO, Fe_2O_3, and SiO_2 remained nearly constant.

The mass transfer during alteration and mineralization was calculated according to the following formula: $\Delta mass = ((1/m) - 1) \times 100$ (Hofstra 1994), where m represents the slope of the regression line of the immobile elements. The calculation results show a mass gain of 4% (Fig. 8a) for siltstone and a mass loss of 16% (Fig. 8b) for limestone, The calculation results indicate that the modification and alteration in the SBT were much more intensive than that in P_3l^1.

6.2 Fluid inclusion petrography

Main-ore- and late-ore-stage quartz and late-ore-stage fluorite were selected for fluid inclusion analysis. Four types of fluid inclusions have been identified based on the characteristics of the fluid inclusions at room temperature (~ 20 °C), the transition characteristics during cooling and heating runs, and their Raman spectra.

Type-I includes mono- or two-phase, liquid-rich aqueous inclusions that are typically lighter in color. This type of inclusion is abundant and commonly coexists with other types of inclusions in main-ore-stage quartz (Fig. 9a, b, f, h) and rare in late-ore-stage quartz and fluorite (Fig. 9c). It typically occurs with an isolated and scattered distribution in quartz and has square, elongated, and negative crystals and irregular shapes, with sizes from 3 to 30 μm. These inclusions can be classified into two subtypes based on their phase state, including type-Ia and type-Ib. Type-Ia is two-phase H_2O-rich aqueous inclusions with 5–15 vol% vapor bubbles at room temperature (Fig. 9a–c). Some type-Ia fluid inclusions decrepitated at temperatures from 190 to 260 °C, and most of these fluid inclusions are homogenized to the liquid phase. Type-Ib is mono-phase aqueous inclusions (Fig. 9c).

Type-II includes two- or three-phase, liquid-rich CO_2–H_2O inclusions with oval, triangle, and irregular shapes. This type of inclusion is mainly in main-ore-stage quartz and occasionally occurs in late-ore-stage quartz and fluorite. Type-II is 10–40 μm in diameter and is commonly larger than other types. According to the CO_2-bearing

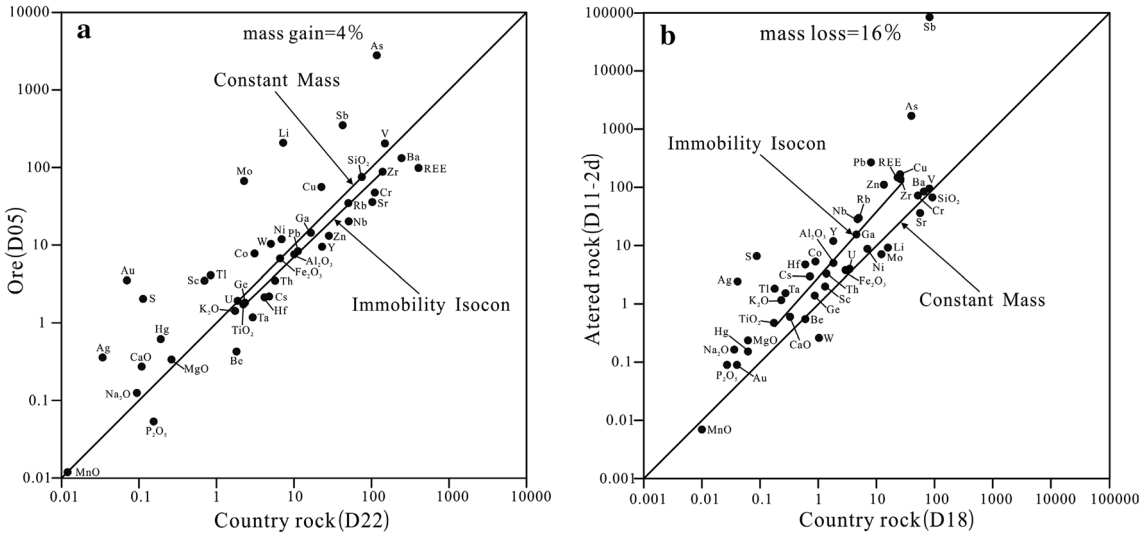

Fig. 8 Logarithmic isocon plots showing the elemental fluxes and mass transfer associated with mineralization between the wall rock and mineralized (altered) rock. The locations of all samples are shown in Fig. 2

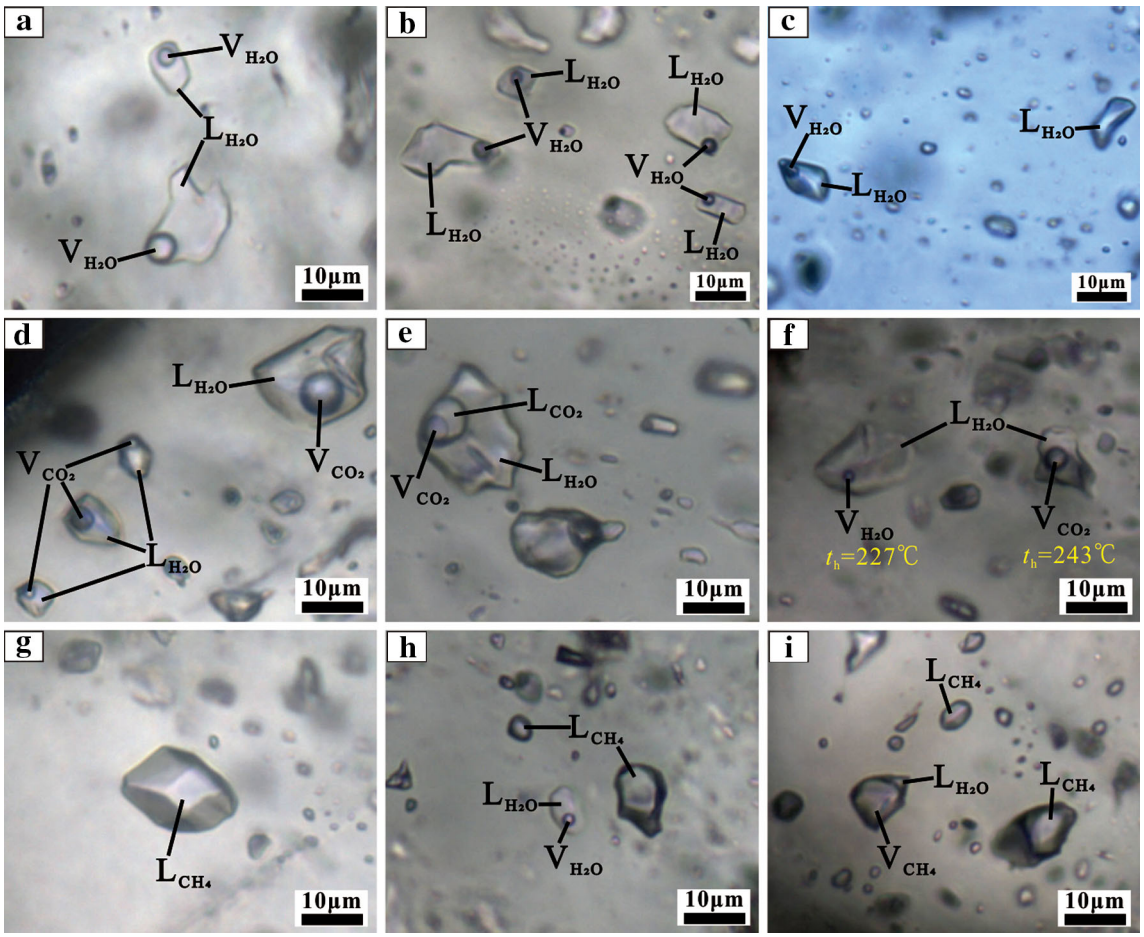

Fig. 9 Microphotographs of fluid inclusions from the Baogudi gold district: **a** two-phase aqueous inclusions (type-Ia) in quartz; **b** two-phase aqueous inclusions (type-Ia) in fluorite; **c** two-phase aqueous inclusions (type-Ia) coexisting with mono-phase aqueous inclusions (type-Ib) in quartz; **d** two-phase CO_2–H_2O inclusions (type-IIa); **e** three-phase CO_2–H_2O inclusions (type-IIb); **f** two-phase CO_2–H_2O inclusions (type-IIa) coexisting with two-phase aqueous inclusions (type-Ia); **g** mono-phase liquid CH_4 inclusions (type-III); **h** mono-phase liquid CH_4 inclusions (type-III) coexisting with two-phase aqueous inclusions; **i** mono-phase liquid CH_4 inclusions coexisting with two-phase CH_4–H_2O inclusions (type-IV). **a**, **c**, **e**–**i** quartz of the main-ore stage; **b** fluorite of the late-ore stage; **d**, **i** quartz of the late-ore stage. L_{H2O}-liquid H_2O, V_{H2O}-vapor H_2O, L_{CO2}-liquid CO_2, V_{CO2}-vapor CO_2, V_{CH4}-vapor hydrocarbon CH_4

phase nature, these inclusions can be divided into two subtypes, including type-IIa and type-IIb. Type-IIa inclusions consist of vapor CO_2 and liquid H_2O and occur together with type-Ia inclusions with a relatively small vapor bubble (Fig. 7d, f). Type-IIb inclusions are composed of liquid plus a vapor CO_2 phase and a liquid H_2O phase at room temperature (Fig. 9e).

Type-III inclusions are mono-phase, pure-liquid CH_4 inclusions (Fig. 9g–i). This inclusion type commonly occurs in main-ore-stage quartz and appear locally in late-ore-stage quartz and fluorite. It generally occurs as oval, round, polygon, and negative crystals and as irregular shapes, varying from 3 to 25 μm in size, with dark edges and a shiny center due to their strong translucency.

Type-IV inclusions are two-phase CH_4–H_2O inclusions (Fig. 9h). This type of inclusion is rare and is comprised of a liquid aqueous phase and a vapor hydrocarbon phase. The volume of the vapor phase ranges from 5 to 95%. They are typically 2–20 μm in diameter with oval, elongated, and negative crystal shapes. This type of inclusion usually coexists with type-III inclusions in main-ore-stage quartz.

6.3 Laser Raman spectroscopic analysis

The gas compositions of various inclusions in quartz were measured using laser Raman spectroscopy. The spectral data reveal that the vapor phase of the two-phase aqueous (type-Ia) inclusions is dominated by H_2O (Fig. 10a) and that most inclusions contain CH_4, CO_2, and N_2 along with H_2O (Fig. 10b). In addition to CO_2, CH_4, and N_2 are identified in CO_2–H_2O inclusions (type-IIa) (Fig. 10c), which is consistent with the fact that the final melting temperature of solid CO_2 (Tm, CO_2) is lower than the standard triple point (56.6 °C) of pure CO_2. The vapor

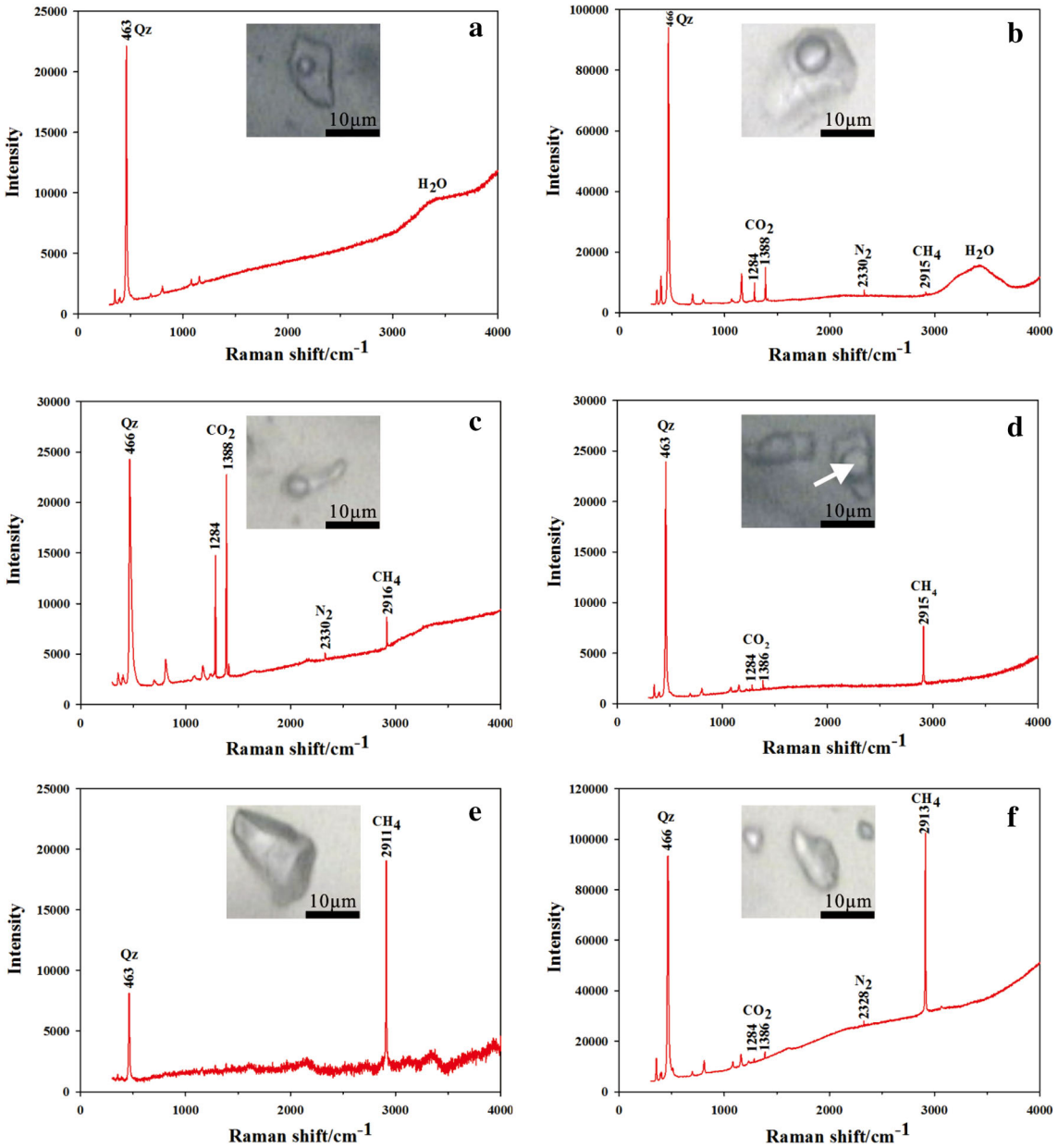

Fig. 10 Laser Raman spectra of fluid inclusions in quartz from the main-ore stage (**a**–**c**, **e**) and late-ore stage (**d**, **f**). **a** Vapor phase of two-phase aqueous inclusions (type-Ia) containing H_2O; **b** vapor phase of two-phase aqueous inclusions (type-Ia) mainly consisting of CO_2, CH_4 and N_2; **c** vapor phase of CO_2–H_2O inclusions (type-IIa) composed of CO_2, N_2 and CH_4; **d** vapor phase of hydrocarbon-H_2O inclusions (type-IV) comprised of CH_4, CO_2 and N_2; **e** mono-phase liquid hydrocarbon inclusions (type-III) containing mostly CH_4; **f** mono-phase liquid hydrocarbon inclusions (type-III containing CO_2 and N_2 in addition to CH_4)

phase of CH_4–H_2O inclusions (type-IV) is dominated by CH_4 and contains minor CO_2 (Fig. 10d). The mono-phase liquid hydrocarbon inclusions (type-III) contain pure CH_4 (Fig. 10e), and some of them also contain small amounts of CO_2 and N_2 (Fig. 10f).

In general, the fluid inclusion types in quartz from the main-ore stage are very rich. In addition to aqueous inclusions (type-I) and CO_2–H_2O inclusions (type-II), abundant CH_4 inclusions (type-III) and CH_4–H_2O inclusions (type-IV) are also commonly detected. In comparison, fluid inclusions in quartz and fluorite of the late-ore stage are dominated by aqueous inclusions (type-I), while both CO_2–H_2O inclusions (type-II) and hydrocarbon inclusions (type-III, type-IV) are relatively rare. Thus, from the main-ore to late-ore stages, the contents of CO_2 and CH_4 in the ore-forming fluid gradually decreased, and the ore-forming fluid underwent an evolution process from H_2O–NaCl–CO_2–CH_4 ± N_2 to H_2O–NaCl ± CO_2 ± CH_4.

6.4 Microthermometric results

Although type-Ib, type-III, and type-IV inclusions occur in quartz and fluorite, their small sizes make it difficult to measure the phase transformation temperatures. Therefore, only the microthermometric data of type-Ia and type-II inclusions are reported here. The salinities of the aqueous fluid inclusions (type-Ia) and CO_2–H_2O inclusions (type-II) were calculated from the final melting temperatures of ice ($T_{m,ice}$) and CO_2 clathrate ($T_{m,cla}$) using the formulas proposed by (Potter et al. 1978) and (Collins 1979), respectively. The microthermometric data are summarized in Table 1 and Fig. 11.

For two-phase aqueous inclusions (type-Ia) from the main- to late-ore stages, the homogenization temperatures (T_h) range from 138 to 270 °C (mostly 180–260 °C) and from 85 to 227 °C (mostly 120–200 °C), with average values of 222 °C and 140 °C, respectively. The freezing point temperatures ($T_{m,ice}$) range from − 5.9 to − 1.6 °C (mean: − 3.1 °C) and from − 5.2 to − 0.2 °C (mean: − 2.4 °C), respectively, corresponding to the salinities of 2.74–9.08 wt% NaCl equiv (mean: 5.07 wt% NaCl equiv) and 0.18–8.14 wt% NaCl equiv (mean: 2.91 wt NaCl equiv), respectively.

For the CO_2–H_2O inclusions (type-II) from the main- to late-ore stages, the final melting temperatures of solid CO_2 ($T_{m,CO2}$) range from − 63.1 to − 57.0 °C (mean: 58.2 °C) and from − 57.7 to − 56.9 °C (mean: 57.3 °C), temperatures which are lower than the standard triple point (− 56.6 °C) of pure CO_2, suggesting that the CO_2 phase may contain CH_4, N_2, and/or other volatiles in addition to CO_2. The $T_{m,cla}$ varies from 6.0 to 10.6 °C (mean: 9.6 °C) and from 7.4 to 10.2 °C (mean: 9.5 °C), corresponding to salinities of 0–7.48 wt% NaCl equivalent (mean: 0.95 wt% NaCl equivalent) and 0–5.05 wt% NaCl equivalent (mean: 1.08 wt% NaCl equivalent), respectively. A few $T_{m,cla}$ values are slightly higher than 10 °C, further suggesting the presence of other volatiles in the CO_2 phase (Zheng 2017). Homogenization of the CO_2 was always toward the liquid phase between 17.2 and 21.9 °C (mean: 19.9 °C) and between 19.8 and 23.2 °C (mean: 21.4 °C). The T_h of the CO_2–H_2O inclusions ranges from 150 to 300 °C (mean: 240 °C) and from 191 to 253 °C (mean: 217 °C), with peaks at 200–260 °C and 180–240 °C, respectively.

Collectively, the ore-forming fluids are characterized by intermediate to low temperatures and low salinity, and the homogenization temperatures and salinities slightly decrease accompanying hydrothermal activity.

Table 1 Microthemometric data of fluid inclusions from the Baogudi gold district

Host minerals/mineralization stage	Inclusion types	Th (°C)		Tm, ice (Tm, cla) (°C)		Tm, CO_2 (°C)		Th, CO_2 (°C)		Salinity (wt%)	
		Range (no.)	Mean	Range (no.)	Mean	Range (no.)	Mean	Range (no.)	Mean	Range (no.)	Mean
Quartz/ore stage	Type-Ia	138–270 (52)	221.7	−5.9 to −1.6 (60)	−3.1					2.74–9.08 (60)	5.07
	Type-II	150–300 (50)	239.5	6.0–10.6 (55)	9.6	−63.1 to −57.0 (21)	−58.2	17.2–21.9 (16)	19.9	0.00–7.48 (55)	0.95
Quartz/late-ore stage	Type-Ia	85–177 (23)	141.1	−5.2 to −0.2 (32)	−2.4					0.35–8.14 (32)	3.88
	Type-II	191–253 (7)	217.4	7.4–10.2 (28)	9.5	−57.7 to −56.9 (10)	−57.3	19.8–23.2 (5)	21.4	0.00–5.05 (28)	1.08
Fluorite/late-ore stage	Type-Ia	97–227 (54)	139	−2.7 to −0.1 (27)	−1.1					0.18–4.49 (27)	1.85

Th = the homogenization temperature; Tm, ice = the final ice melting temperature; Tm, cla = the temperature of CO_2 clathrate melting; Tm, CO_2 = the melting temperature of drikold; Th, CO_2 = the temperature of CO_2-phase homogenization; salinity = calculated salinity (wt% NaCl equivalent)

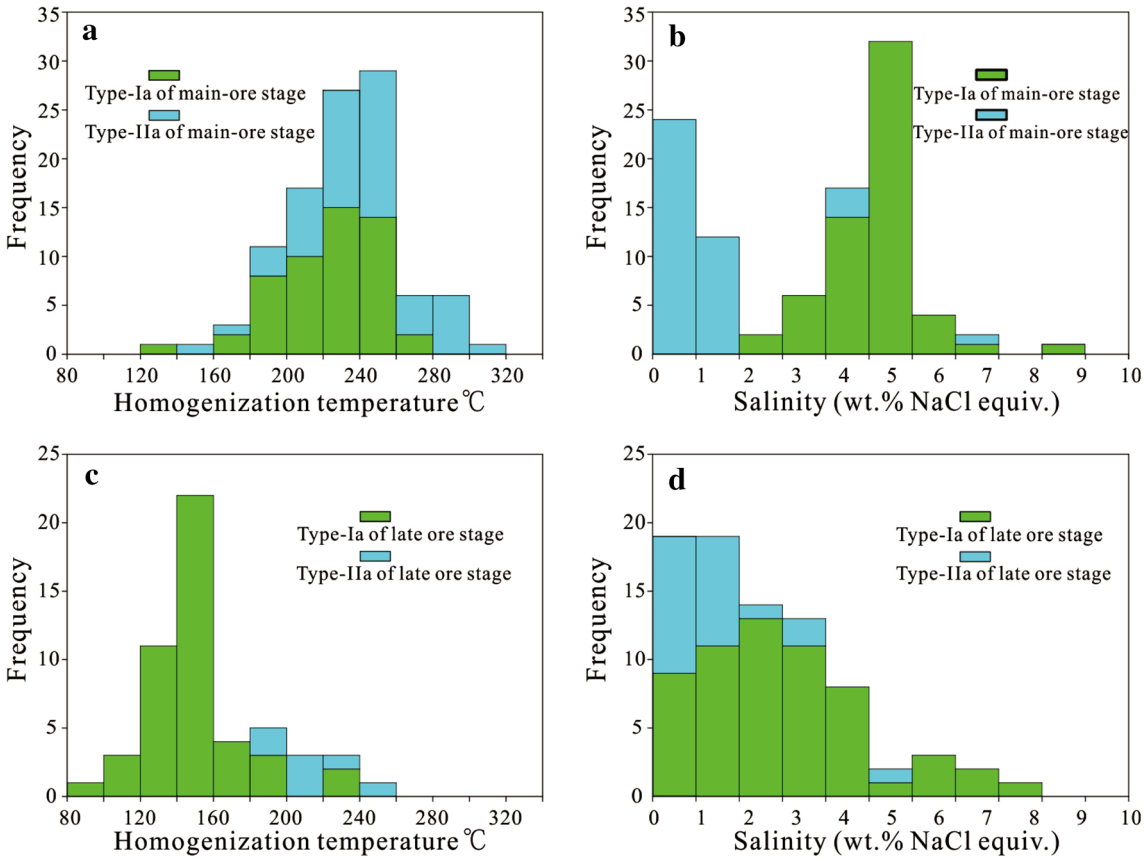

Fig. 11 Frequency histograms showing the homogenization temperatures (**a**, **c**) and calculated salinities (**b**, **d**) of fluid inclusions from the main-ore stage (**a**, **b**) and late-ore stage (**c**, **d**)

Table 2 Hydrogen, oxygen, carbon, and sulfur isotopic compositions of the Baogudi gold district

Sample no.	Mineral	δD_{SMOW} (‰)	$\delta^{18}O_Q$ (‰)	$\delta^{18}O_{SMOW}$ (‰)	$\delta^{13}C_{PDB}$ (‰)	T (°C)	Mineral	$\delta^{34}S_{CDT}$ (‰)
D01-2	Quartz	− 59.2	11.2	22.3	− 9.8	209		
D04-2b	Quartz	− 68.9	8.0	19.1		209		
D06-4a	Quartz	− 55.7	13.5	23.0	− 9.4	239		
D10-3	Quartz	− 61.6	5.9	19.0	− 9.1	179	Stibnite	− 0.6
D11-2a	Quartz	− 70.8	4.5	20.8	− 13.3	142	Stibnite	1.9
D13-3	Quartz	− 76	9.1	18.6		239		
D15-3b	Quartz	− 68.4	15.0	24.5	− 14.3	239		
D19-1	Quartz	− 60.9	8.5	22.3	− 7	171	Stibnite	− 0.4
D24b	Quartz	− 64.8	12.7	22.2	− 10.2	239		
D27-2b	Quartz	− 64	14.0	23.4	− 14.3	239		
D32-1	Quartz	− 63.1	7.0	16.5	− 12.3	239		

6.5 Stable isotope compositions

The analytical or calculated hydrogen, oxygen, and carbon isotopic compositions of quartz from the main- and late-ore stages and the sulfur isotopic compositions of late-ore stibnite are presented in Table 2. The analyzed hydrogen isotopic compositions of the inclusion waters (δDH_2O) from ore-related quartz vary from − 76 to − 55.7‰, with an average of − 64.9‰. The $\delta^{18}O$ values of the quartz ($\delta^{18}OQz$) range from 16.5 to 24.5%, with a mean of ~ 21.1‰. Based on the measured $\delta^{18}O$ value of quartz from the mineralization stage, the $\delta^{18}O$ values of the ore-

forming fluid were calculated using the quartz-water fractionation equation ($1000\ln\alpha Qz - W = 3.38 \times 106/T^2 - 3.40$) (Clayton et al. 1972), where the average homogenization temperature of the two-phase aqueous inclusions is taken as the quartz formation temperature. The calculated $\delta^{18}O$ values of the mineralizing fluids ($\delta^{18}OH_2O$) vary from 4.5 to 15.0‰, with an average of 10.0‰. The fluid inclusion water in quartz has strongly negative $\delta^{13}C$ values, ranging from − 14.3 to − 7.0‰, with a mean of about − 11.1‰. The $\delta^{34}S$ values of stibnite vary from − 0.6 to 1.9‰, with average values of 0.3‰.

7 Discussion

7.1 Element migration and mineralization

Though Carlin-type gold metallogenic systems in southwest Guizhou are characterized by close Au–Hg–Sb–As–Tl association on the regional scale (Hu et al. 2002; Large et al. 2011), various gold deposits exhibit differences, such as Lannigou with Au–As–Cu–Tl–Sb and Xiongwu with Au–As–Hg–U (Zhang et al. 2003). In the Baogudi gold district, mass transfer associated with alteration and mineralization shows that elemental assemblages, including Au, As, Sb, Hg, and Tl, were added to altered rocks during the main-ore stage, which is similar to the case for many Carlin-type gold deposits in southwest Guizhou such as Shuiyindong and Jiadi (Xia et al. 2010; Hu et al. 2018a, b). Permian sediments in southwest Guizhou had low concentrations of Au and associated elements (Zhou et al. 2009; Hu et al. 2018a). Moreover, taking into account that the ore fluids of Carlin-type gold deposits in southwest Guizhou contain high concentrations of Carlin-suite elements (120 ppm As, 20 ppm Sb, and 3–5 ppm Au) (Su et al. 2009). Thus, these paragenetic elements in the main-ore stage might have been provided by the hydrothermal fluid that also offered metallogenic material for other gold deposits in southwest Guizhou. Remarkably, As, Sb, and Tl were added to the mineralized rocks during the late-ore stage, whereas Au and Hg remained nearly constant, indicating that ore-forming elemental separation occurred in this stage. This phenomenon can be explained by the mineralization process having undergone a single successive stage, resulted in depleted Au and Hg concentrations in the late-ore stage. These Carlin-suite elements, which were enriched in the late-ore stage (such as As and Sb), typically form sulfides such as stibnite, realgar, and orpiment (Figs. 4e–g, 5j–k). This implies that Carlin-suite elements, including As, Sb, Hg, and Tl, in addition to Au, can serve as "geochemical signatures" of mineralization.

In addition to the specific suite of trace elements of Au–Hg–Sb–As–Tl, Mo was also added to the mineralized siltstone of the P_3l^1. This is similar to the case in some other typical gold deposits, such as high Mo in gold-rich ores of Getang (∼ 110 ppm) and Nibao (∼ 400 ppm) (Zhang et al. 2003). In comparison, the silicified limestone of the SBT in the Baogudi district shows a slight decrease in Mo (Fig. 8). Collectively, the enrichment characteristics of Mo are similar to those of Au and Hg, suggesting that Au, Hg, and Mo were relatively active in the early stage and then reduced. However, there might be a different possibility in that the higher Mo contents could indicate a mafic provenance, as Zhang et al. (2003) suggested.

Although obvious pyritization and arsenopyritization were observed in mineralized (altered) rocks, mass transfer associated with alteration and mineralization indicates that Fe was not added during Au mineralization. Su et al. (2009) reported that the original ore-forming fluids were Fe-poor (< ∼ 400 ppm); however, the host rocks were Fe rich, exhibited by characteristics such as ferroan carbonate minerals containing up to 7.0 wt% Fe. Thus, they concluded that the iron in pyrite and arsenopyrite was probably from the dissolution of ferroan carbonate in the country rock. This is consistent with the petrographic observation that arsenian pyrite and arsenopyrite occur with dolomite (Fig. 5g–h). Moreover, the S enriched into the original ore-forming fluids (Su et al. 2009) was also added to the mineralized (altered) sample. Thus, arsenian pyrite and arsenopyrite might have precipitated as S- and As-bearing ore fluids, which reacted with Fe-rich sedimentary rocks.

Whether sulfur and iron were introduced into the mineralized rock together or independently can be effectively determined using the correlation diagrams of the iron and sulfur contents (Stenger et al. 1998). Figure 12 shows that three SBT samples plotted above the pyrite line, probably because these three samples contained more other sulfides

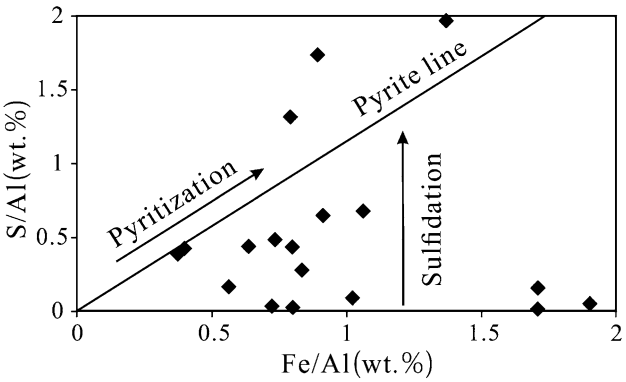

Fig. 12 Correlation diagrams showing the relations between iron and the total sulfur normalized to immobile Al (Hofstra 1994). The arrows show the directions of compositional changes associated with pyritization (addition of sulfur and iron) and sulfidation (addition of sulfur). The line of pyrite is based on the relative contents of sulfur and iron in pyrite: S = 1.15 × Fe (wt%) (Stenger et al. 1998)

in addition to pyrite, such as stibnite, realgar, and orpiment. In contrast, other samples plotted below the pyrite line, suggesting that the sedimentary rocks contained more iron than is needed to form pyrite. This further indicates that iron was probably derived from the sedimentary rock. The black arrows in Fig. 12 show the paths of pyritization and sulfidation. The Baogudi sample plot generally extends upward toward the arrow of sulfidation, similar to other typical Carlin-type gold deposits in southwest Guizhou (Tan et al. 2015a). This suggests that the sulfidation of immobile host-rock Fe by the introduced S and associated metallogenic elements (Au, As, Hg, Tl, and Sb) to form sulfides might be the principal precipitation mechanism of the ore.

Almost all altered samples, including mineralized siltstone and limestone, show obvious silicification. Although silicification is judged to be associated with the formation of mineralization in southwest Guizhou (Cline et al. 2013; Tan et al. 2015a), in the Baogudi gold district, there is no significant correlation between the concentrations of Carlin-suite elements and the degree to which the host rocks have undergone silicification. In particular, SiO_2 remains nearly constant in the mineralization limestone of the SBT. This suggests that the silicification range is much larger than the mineralization area.

7.2 Source of the ore-forming fluids

The sulfur isotopic compositions of sulfide minerals depend on the total sulfur composition of the hydrothermal fluid as well as the physical and chemical conditions (oxygen fugacity, pH, ionic strength, and temperature) of the ore-forming fluid evolution (Ohmoto 1972). Pyrite, stibnite, and other sulfides are the dominant hydrothermal minerals formed during Au mineralization. The mineral assemblage, combined with the presence of abundant hydrocarbon components in fluid inclusions, suggests a reducing ore fluids system (Chen et al. 2017). Additionally, the microthermometric measurements show ore fluid temperatures of ~ 200 °C. The S isotope fractionation between sulfide minerals and hydrothermal fluids is small at that temperature (Ohmoto 1972). Thus, sulfides precipitating from the hydrothermal fluid should have $\delta^{34}S$ values similar to the $\delta^{34}S_{\sum S}$ (Ohmoto and Goldhaber 1997). Collectively, the $\delta^{34}S$ values of stibnite (between− 0.6 and 1.9‰) can represent the bulk sulfur isotopic composition of the initial ore-forming fluid in the Baogudi gold district.

As shown in Fig. 13, the S isotopic compositions of the ore pyrite rim and arsenopyrite obtained by in situ measurements and other ore-related sulfide minerals from all deposits, except Lannigou, have very similar $\delta^{34}S$ values, and most of these data plot between ~ − 5 and +5‰. Lannigou exhibits a broad range of values for S in sulfide

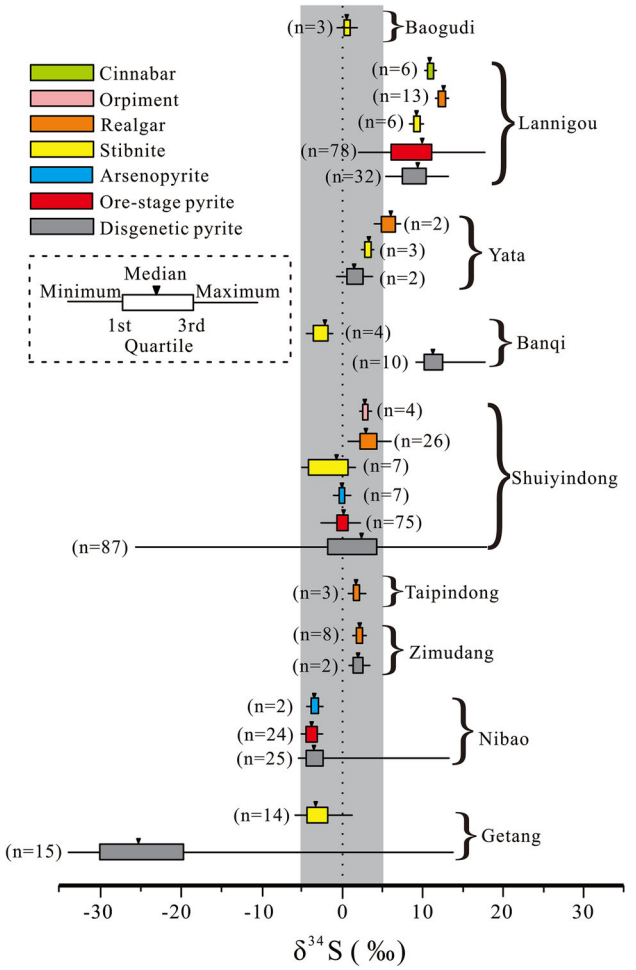

Fig. 13 $\delta^{34}S$ isotopic ratio data of pre-ore-stage pyrites, ore-stage pyrites, arsenopyrite, stibnite, realgar, and orpiment from various Carlin-type gold deposits of the platform area in southwest Guizhou (data are from Li et al. 1989; Liu et al. 1994; Zhang et al. 2003, 2010; Xia 2005; Wang et al. 2013; Fan 2015; Tan et al. 2015b; Hou et al. 2016; Wei 2017; Zheng 2017; Xie et al. 2018; Yan et al. 2018; this study)

minerals, and the associated samples are more enriched in higher $\delta^{34}S$ values than those from other Guizhou Carlin-type gold deposits. However, the Lannigou $\delta^{34}S$ values of the pyrite As-rich rim (1.1–7.9‰, most data < 5‰) determined by in situ NanoSIMS may represent the S isotopic signature of the initial ore fluids (Yan et al. 2018; Xie et al. 2018), and these values are also consistent with those of other Guizhou Carlin-type gold deposits. The $\delta^{34}S$ values of stibnite (− 0.6 to 1.9‰) from Baogudi are within the range of ore-related sulfide minerals from seven classic Guizhou Carlin-type gold deposits (− 5 to 5‰). These relatively consistent $\delta^{34}S$ values are very close to the values of mantle sulfur (0–3‰) (Chaussidon and Lorand 1990). Furthermore, recent gravity and magnetic investigations have recognized a number of probable buried intermediate-acid intrusions in southwestern Guizhou

(Fig. 1) (Liu et al. 2017; Wang et al. 2015). Thus, we propose that a magmatic hydrothermal fluid with a $\delta^{34}S$ value close to the mantle value (i.e., close to zero) is the candidate for the source of sulfur. On the other hand, the Baogudi gold is hosted in the Maokou and Longtan Formations of the Permian age. The $\delta^{34}S$ values of marine sulfate at that time are 10–15‰ (Holser and Kaplan 1966; Claypool et al. 1980). The homogenization temperature of the hydrothermal fluids in Baogudi is ~ 200 °C, under which the sulfate-sulfide fractionation associated with thermochemical sulfate reduction is 0–10‰ (Kiyosu 1980; Krouse et al. 1988). Consequently, the resulting $\delta^{34}S$ values determined by thermochemical sulfate reduction range from 0 to 15‰ for these sulfides. Therefore, it is possible that reduced marine sulfate was an alternative source of sulfur.

The δD_{H2O} and $\delta^{18}O_{H2O}$ of the fluid inclusions in ore-stage quartz from the Baogudi gold district have a broad range. The $\delta^{18}O_{H2O}$ value is significantly greater than the values of tunnel water, river water, and spring water from southwestern Guizhou (Tan et al. 2017b), whereas it is close to the $\delta^{18}O_{H2O}$ values of magmatic water, which range from 5 to 7‰ (Zheng and Chen 2000), or of mantle-derived fluids, which vary from 6 to 10‰ (Liu et al. 2001). Likewise, most of the δD_{H2O} values overlap with the value of magmatic water, ranging from− 80 to− 50‰ (Zheng and Chen 2000), but they are significantly greater than the average δD_{H2O} value of local meteoric water (− 85‰) (Han et al. 1999).

Hydrogen and O isotopes of quartz from the Baogudi gold district and seven typical Carlin-type gold deposits in southwest Guizhou are plotted in Fig. 14. The H and O isotopic values of quartz from these typical Carlin-type gold deposits were relatively dispersed, with almost all plots located below the field of metamorphic water and many lying in the field of formation fluids, as well as close to the meteoric water line. This indicates that the ore-forming fluids might have been mainly basinal in origin. Additionally, a small fraction of plots falls within the field of magmatic water or close to its boundary, possibly indicating that magmatic origin only played a minor role. However, our study in Baogudi showed that a substantial fraction of samples plotted within or close to the field of magmatic water, while other points fell within or below the field of metamorphic water. Since the possibility of predominant metamorphic origin can be excluded because of the absence of regional metamorphism (Hu et al. 2018a), we propose that the ore-forming fluids might have mainly been derived from a magmatic fluid.

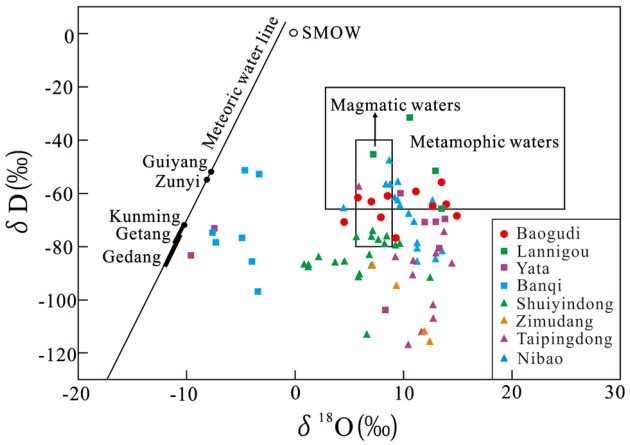

Fig. 14 Hydrogen and oxygen isotopic compositions of ore-forming fluids based on analyses of quartz from various Carlin-type gold deposits of the platform area in southwest Guizhou (data are from Li et al. 1989; Zhu et al. 1998; Hu et al. 2002; Pang et al. 2005; Xia 2005; Wang et al. 2013; Peng et al. 2014; Xie et al. 2016; Tan et al. 2015a, b; this study)

There are mainly three distinct reservoirs of C, including marine carbonates, mantle or magma carbon, and biogenetic organic matter (Cai et al. 2018). Marine carbonates are isotopically heavy, with a mean $\delta^{13}C_{PDB}$ value of ~ 0‰ (Veizer et al. 1980). Mantle or magma carbon has an isotopic composition ranging from− 8 to− 5‰ (Cartigny et al. 2001), and the $\delta^{13}C_{PDB}$ of biogenetic organic matter hosted in sedimentary rocks and of graphite hosted in metamorphic rocks or magmatic rocks is generally lower than− 20‰ (Hoefs 2009). The $\delta^{13}C_{PDB}$ values of fluid inclusions in the Baogudi district range from − 14.3 to− 7‰ and are close to those of the mantle, indicating a deep mantle source. However, the possibility that the carbon in the ore fluids could have been derived from a mixture of different carbon reservoirs cannot be eliminated.

7.3 Comparison of the Baogudi gold district with typical Carlin-type gold deposits in southwest Guizhou

Table 3 summarizes the comparison between Baogudi and typical Carlin-type gold deposits in southwest Guizhou. Even though the proven gold reserves within the Baogudi gold district are small compared with economic Carlin-type gold deposits in Southwest Guizhou, the newly discovered Baogudi gold district shows many critical characteristics that define the Guizhou Carlin-type gold deposits (Table 3). Similarities include the following. (1) Mineralization is controlled by the lithology and structure. Faults and folds, which are characterized by structure combinations appearing as “a strike fault over an anticline”, control the strata-bound and fault-controlled ore bodies, respectively. On the other hand, the carbonate- and megaclast-rich sedimentary rocks of P_3l and the SBT are ideal host rocks for mineralization. (2) Alteration related to mineralization includes sulfidation and silicification, and sulfidation might be the principal precipitation mechanism of

Table 3 Comparison between Baogudi and classic Carlin-type gold deposits in southwest Guizhou

Item	Classic Carlin-type gold deposits in southwest Guizhou	Baogudi gold district
Ore-bearing stratum	Upper Permian to Triassic formation in the platform-face area (Shuiyindong, Zimudang, Getang, Xiongwu, Nibao, Jiadi, etc.), middle Triassic formation in the basin-face area (Lannigou, Banqi, and Yata, etc.)	Longtan formation and the SBT
Host rock	Bioclastic limestone, calcareous siltstones, and basaltic rocks or basaltic pyroclastic rocks	Carbonate- and megaclast-rich sedimentary rocks
Ore-controlling structure	Anticlines or domes, high-angle reverse faults	Baogudi anticlinorium and axial reverse faults
Ore body type	Stratabound orebodies and fault-controlled orebodies	Stratabound orebodies with stratiform, stratoid or lenticular shapes; fault-controlled type with vein or lens shapes
Hydrothermal alteration	Sulfidation, silicification, decarbonation, dolomitization, calcilization, fluoritization, and argillization	Sulfidation, silicification, calcification, fluoritization, dolomitization, and decarbonation
Mineral assemblage	Quartz, pyrite, arsenopyrite, stibnite, realgar, orpiment, fluorite, and clay minerals	Main-ore stage: quartz + arsenian pyrite + arsenopyrite, late-ore stage: quartz + stibnite + fluorite ± orpiment ± realgar
Ore-forming element association	Au, As, Tl, Hg, and Sb (Shuiyindong and Zimudang); Au, As, Tl, Hg, Sb, and Mo (Getang and Nibao); Au, As, Tl, Sb, and Cu (Lannigou); Au, As, Hg, and U (Xiongwu)	Main-ore stage: Au, As, Tl, Hg, and Sb; late-ore stage: As, Sb, and Tl
Ore-forming fluid	Intermediate to low temperatures (190–300 °C), low salinity (1.6–3.3% NaCl equivalent), CO_2-rich vapor component (6.3–8.4 mol% CO_2 as well as minor CH_4 and trace N_2), ultrahigh trapping pressures (0.5–2.3 kbar); formation depth of 1.5–4.3 km (Shuiyindong, Lannigou, Yata)	Main-ore stage: final homogenization temperatures mostly from 180 to 260 °C and salinity from 0 to 9.08% NaCl equivalent; Late-ore stage: final homogenization temperatures mostly from 140 to 220 °C and salinity from 0 to 7.74% NaCl equivalent. Ore-forming fluid contain abundant H_2O, CO_2, CH_4, and minor N_2
Stable isotope characteristics	Hydrogen and oxygen isotopes values of quartz and clay minerals, with almost all plotted below the field of metamorphic water and many lying in the field of formation fluids, as well as close to the meteoric water line (Shuiyindong, Zimudang, Nibao, Lannigou, Banqi, and Yata). The $\delta^{13}C$ values from calcites associated with mineralization plot between −3 and −9‰ (Shuiyindong, Zimudang, Nibao). The $\delta^{34}S$ values of ore-related sulfide minerals range from −5 to 5‰ (Shuiyindong, Zimudang, Getang, Nibao, Lannigou, Banqi, and Yata)	The δDH_2O and calculated $\delta^{18}OH_2O$ values of fluid inclusions in quartz range from −76 to −55.7‰ and 4.5 to 15.0‰, respectively. Almost all samples plot within or close to the field of magmatic water, with some points falling within or below the field of metamorphic water. The $\delta^{13}C$ values of inclusion water from quartz plot between −14.3 and −7.0‰. The $\delta^{34}S$ values of stibnite range from −0.6 to 1.9‰
Ore deposit scale	Middle to super-large gold deposits	Small gold deposits and ore occurrences

Li et al. (1989), Liu et al. (1994), Zhu et al. (1998), Hu et al. (2002), Zhang et al. (2003, 2010), Pang et al. (2005, 2014), Xia (2005), Wang et al. (2013), Xie et al. (2017, 2018), Fan (2015), Tan et al. (2015b), Hou et al. (2016), Wei (2017), Zheng (2017), Hu et al. (2018a) and Yan et al. (2018)

ore. (3) The main-ore stage minerals are represented by arsenian pyrite and arsenopyrite, while late-ore stage minerals include stibnite, realgar, orpiment, etc. (4) The Baogudi gold district is accompanied by Au, Hg, Sb, As, and Tl enrichment, which is the hallmark of many typical Carlin-type gold deposits. (5) The ore-forming fluids are characterized by intermediate to low temperatures and low salinity.

Based on the ore geological and geochemical characteristics of the Baogudi gold district, we suggest that the Baogudi gold district is a new potential Carlin-type gold mineralization trend in Southwest Guizhou, China.

7.4 Implications for ore genesis

Although the potential importance of magmatic fluids has long been discounted because of the paucity of igneous intrusions in southwestern Guizhou, our results from S, C, H, and O isotopic analyses in the Baogudi Carlin-type gold district indicate that the ore fluids could have predominantly been derived from magmatic fluid with minor contributions from the strata. Additionally, recent gravity and magnetic studies suggest numerous plutons $\sim$ 5 km below the surface (Fig. 1), which are spatially associated with the pre-existing Carlin-type gold deposits in southwestern Guizhou (include study area) (Liu et al. 2017; Wang et al. 2015). The lack of intrusion outcrops in southwest Guizhou

may be due to a thick section of sedimentary rocks in the region, including a Devonian-Triassic passive margin sequence (6–12 km) (Xie et al. 2018), as well as the relatively shallow denudation depth (Luo and Zeng 2018). Collectively, we favor that the Baogudi gold district and many other Carlin-type gold deposits in southwestern Guizhou are distal products of deep magmatic hydrothermal systems. Likewise, the magmatic-hydrothermal origins of other Carlin-type gold deposits in southwest Guizhou, such as Shuiyingdong, Nibao, Jiadi, and Lannigou, have also been proposed by many researchers in recent years (Hu et al. 2018a, b; Xie et al. 2018; Hu et al.2017; Liu et al. 2017; Yan et al. 2018; Zheng 2017; Tan et al. 2015a, b).

The newly discovered Baogudi gold district and other Guizhou Carlin-type gold deposits share consistently similar geological and geochemical characteristics, including host rocks, ore-controlling structures, ore body geometry, alteration minerals and textures, ore fluid nature and sources, and element associations (Su et al. 2018; Xie et al. 2018). Thus, these deposits most likely formed in response to a single widespread metallogenic event.

S-, As-, Sb-, and Au-rich and Fe-poor and $CO_2 + CH_4$-bearing fluids were potentially released by deep intrusions and ascended along deep faults or fault zones. The rising fluids could further leach the characteristic ore elements of Au, As, Sb, Hg, and Tl from the surrounding strata (Hu et al. 2017). Where ore fluids encountered Fe-bearing carbonate-rich host rocks under appropriate pressure–temperature conditions, ore fluids reacted with Fe-bearing carbonate minerals and sulfidized the Fe, leading to the precipitation of Au-bearing arsenian pyrite and arsenopyrite. Ultimately, this process produces two types of ore bodies. On one hand, the ore-forming fluid migrated vertically along the reverse fault near the anticline axis and formed fault-controlled orebodies. On the other hand, the ore-forming fluid migrated horizontally along the interlayer fracture zones and then converged at the high position of an anticline to form strata-bound orebodies.

8 Conclusions

Detailed studies of the petrography, mineralogy, bulk chemical compositions, microthermometry and compositions of fluid inclusions and of isotopic compositions allow us to draw the following conclusions.

1. The paragenesis of the Baogudi gold district can be divided into three stages, including the sedimentation diagenesis, hydrothermal, and supergene stages. The sedimentation diagenesis stage mainly consists of quartz and pyrite. The hydrothermal stage is divided into the main-ore and late-ore substages. Quartz, arsenian pyrite, and arsenopyrite formed during the main-ore substage, and quartz, stibnite, fluorite, orpiment, and realgar precipitated during the late-ore substage. The supergene stage predominately contains limonite and valentinite.
2. Bulk chemical composition analysis indicates that the Baogudi gold district contains Au and Sb mineralizations, which is similar to the case for classic Carlin-type deposits. Correlation analysis between Fe and S indicates that sulfidation is responsible for ore formation.
3. Four types of fluid inclusions in quartz and fluorite from the Baogudi gold district were identified, namely, aqueous (type-I), CO_2–H_2O (type-II), CH_4 (type-III), and CH_4–H_2O inclusions (type-IV). The main-ore stage fluids contain H_2O, CO_2, CH_4, and minor N_2, with medium to low temperatures (180–260 °C) and low salinity (0–9.08% NaCl equivalent). The late-ore stage fluids consist of H_2O, CO_2, and minor CH_4, with low temperatures (120–200 °C) and low salinity (0–7.48% NaCl equivalent). From the main-ore to late-ore stages, the ore fluid temperature, salinity, and concentrations of CO_2 and CH_4 decreased.
4. The hydrogen, oxygen, carbon, and sulfur isotopic compositions in the Baogudi district consistently indicate that the ore fluid was released from deep intrusions, with minor contributions from strata. Moreover, the Guizhou Carlin-type deposits were likely sourced from the same ore-forming fluids.
5. The Baogudi metallogenic district has numerous characteristics that are typical of Carlin-type gold deposits in southwest Guizhou. The Baogudi gold district and other Carlin-type gold deposits in southwest Guizhou most likely formed in response to a single widespread metallogenic event.

Acknowledgements The authors appreciate Liping Huang for his help during the fieldwork in the Baogudi district. Dr. Heqing Liu and Wendou Dong are thanked for their encouragement and improvements to the manuscript. We are also indebted to Jiali Cai, Shaohua Dong, and Mu Liu for assistance with fluid inclusions, SEM, and element and stable isotopic analyses. Special thanks are given to two anonymous reviewers for their critical comments and suggestions. This study is supported by the National Key R&D Program of Deep-penetrating Geochemistry (2016YFC0600607) and Deep Mineral Resources Exploration and Exploitation (2017YFC0601500), the Geological Research Project of Bureau of Geology and Mineral Exploration and Development Guizhou Province (Qian Di Kuang Ke He (2017) No. 10), and the National Science Foundation of China (Nos. 41802027, 41802088).

References

Cai QR, Yan YF, Yang GS, Fuju J, Chao L (2018) Genesis of the Nanyangtian scheelite deposit in southeastern Yunnan Province, China: evidence from mineral chemistry, fluid inclusions, and C–O isotopes. Acta Geochim 37:1–18

Cartigny P, Jendrzejewski N, Pineau F, Petit E, Javoy M (2001) Volatile (C, N, Ar) variability in MORB and the respective roles of mantle source heterogeneity and degassing: the case of the Southwest Indian Ridge. Earth Planetary Sci Lett 194:241–257

Chaussidon M, Lorand JP (1990) Sulfur isotope composition of orogenic spinel Lherzolite massifs from Ariege (north-eastern pyrenees, France)—an ion microprobe study. Geochim Cosmochim Acta 54:2835–2846. https://doi.org/10.1016/0016-7037(90)90018-g

Chen J, Yang RD, Gao JB, Zheng LL, Du LJ, Yuan MG, Wei HR (2017) Mineralogy, sulfur isotopes and infrared microthermometric study of the Leishan–Rongjiang antimony ore field, SW China. Acta Geochim 36:339–352

Claypool GE, Holser WT, Kaplan IR, Sakai H, Zak I (1980) The age curves of sulfur andoxygen isotopes in marine sulfate and their mutual interpretation. Chem Geol 28:199–260

Clayton RN, Mayeda TK (1963) The use of bromine pentafluoride in the extraction of oxygen from oxides and silicates for isotopic analysis. Geochim Cosmochim Acta 27:43–52

Clayton RN, O'Neil JR, Mayeda TK (1972) Oxygen isotope exchange between quartz and water. J Geophys Res 77:3057–3067

Cline JS, Muntean JL, Gu XX, Xia Y (2013) A comparison of Carlin-type gold deposits: Guizhou Province, Golden Triangle, Southwest China, and Northern Nevada, USA. Earth Sci Front 20:1–18

Coleman ML, Shepherd TJ, Durham JJ, Rouse JE, Moore GR (1982) Reduction of water with zinc for hydrogen isotope analysis. Anal Chem 54:993–995

Collins PL (1979) Gas hydrates in CO_2-bearing fluid inclusions and the use of freezing data for estimation of salinity. Econ Geol 74:1435–1444

Fan J (2015) Study on geochemistry and metallogenic mechanism of the Getang large-scale gold ore deposit Dissertation. Kunming University of Science and Technology Dissertation, pp 1–169 (in Chinese with English abstract)

Finlow-Bates T, Stumpfl EF (1981) The behaviour of so-called immobile elements in hydrothermally altered rocks associated with volcanogenic submarine-exhalative ore deposits. Miner Depos 16:319–328

Grant JA (1986) The isocon diagram—a simple solution to gresens equation for metasomatic alteration. Econ Geol 81:1976–1982. https://doi.org/10.2113/gsecongeo.81.8.1976

Gresens RL (1967) Composition-volume relationships of metasomatism. Chem Geol 2:47–65

Gu XX, Zhang YM, Li BH, Dong SY, Xue CJ, Fu SH (2012) Hydrocarbon-and ore-bearing basinal fluids: a possible link between gold mineralization and hydrocarbon accumulation in the Youjiang basin, South China. Miner Depos 47:663–682 **(in Chinese with English abstract)**

Han ZJ, Wang YG, Feng JZ, Chen TJ, Luo XH, Liu YH (1999) The geology and exploration of gold deposits in southwestern Guizhou: China. Guizhou Science and Technology Press, Guiyang, pp 1–146 **(in Chinese with English abstract)**

Hoefs J (2009) Stable isotope geochemistry. Springer, Berlin

Hofstra AH (1994) Geology and genesis of the Carlin-type gold deposits in the Jerritt Canyon district, Nevada. Dissertation, University of Colorado

Hofstra AH et al (2005) Source of ore fluids in Carlin-type gold deposits, China: implications for genetic models. Miner Depos Res Meet Glob Chall. https://doi.org/10.1007/3-540-27946-6_137

Holser WT, Kaplan IR (1966) Isotope geochemistry of sedimentary sulfates. Chem Geol 1:93–135

Hou L et al (2016) Textures and in situ chemical and isotopic analyses of pyrite, Huijiabao Trend, Youjiang Basin, China: implications for paragenesis and source of sulfur. Econ Geol 111:331–353. https://doi.org/10.2113/econgeo.111.2.331

Hu RZ, Su WC, Bi XW, Tu GZ, Hofstra AH (2002) Geology and geochemistry of Carlin-type gold deposits in China. Miner Depos 37:378–392. https://doi.org/10.1007/s00126-001-0242-7

Hu RZ et al (2017) The giant South China Mesozoic low-temperature metallogenic domain: reviews and a new geodynamic model. J Asian Earth Sci 137:9–34. https://doi.org/10.1016/j.jseaes.2016.10.016

Hu XL, Gong YJ, Zeng GP, Zhang ZJ, Wang J, Yao SZ (2018a) Multistage pyrite in the Getang sediment-hosted disseminated gold deposit, southwestern Guizhou Province, China: Insights from textures and in situ chemical and sulfur isotopic analyses. Ore Geol Rev 99:1–16. https://doi.org/10.1016/j.oregeorev.2018.05.020

Hu XL, Zeng GP, Zhang ZJ, Li WT, Liu WH, Gong YJ, Yao SZ (2018b) Gold mineralization associated with Emeishan basaltic rocks: mineralogical, geochemical, and isotopic evidences from the Lianhuashan ore field, southwestern Guizhou Province, China. Ore Geol Rev 95:604–619. https://doi.org/10.1016/j.oregeorev.2018.03.016

Kesler SE et al (2003) Evaluation of the role of sulfidation in deposition of gold, Screamer section of the Betze-Post Carlin-type deposit, Nevada. Econ Geol Bull Soc Econ Geol 98:1137–1157. https://doi.org/10.2113/98.6.1137

Kiyosu Y (1980) Chemical reduction and sulfur-isotope effects of sulfate by organic matter under hydrothermal conditions. Chem Geol 30:47–56

Krouse HR, Viau CA, Eliuk LS, Ueda A, Halas S (1988) Chemical and isotopic evidence of thermochemical sulfate reduction by light hydrocarbon gases in deep carbonate reservoirs. Nature 333:415–419

Kuang Z, Long SQ, Cao YR, Huang XX, Wu XF (2012) The relationship between remote sensing structures and gold deposits and ore-prospecting prognosis in southwest Guizhou. Remote Sens Land Resour 24:160–165 **(in Chinese with English abstract)**

Large RR, Bull SW, Maslennikov VV (2011) A carbonaceous sedimentary source-rock model for Carlin-type and orogenic gold deposits. Econ Geol 106:331–358. https://doi.org/10.2113/econgeo.106.3.331

Li WK, Jiang XS, Ju RH, Meng FY, Zhang SX (1989) The geological characteristics and metallogenesis of disseminated gold deposits in southwestern Guizhou. China. Geological Publishing House, Beijing, pp 1–86 **(in Chinese)**

Liu JZ (2003) Ore Characteristics and gold occurrence of the Shuiyindong gold deposit, Guizhou. Gui Zhou Geol 20:30–34 **(in Chinese with English abstract)**

Liu DS, Tan YJ, Wang JY, Wei LM, Jiang SF (1994) Carlin-type gold deposit in China. Nanjing University Press, Nanjing, pp 1–414 **(in Chinese)**

Liu CQ, Huang ZL, Li HP, Su GL (2001) The geofluid in the mantle and its role in ore-forming processes. Earth Sci Front 4:000

Liu JZ et al (2009) Researches on the SBT of Shuiyindong gold Deposit and significance for regional prospecting. Gold Sci Technol 17:1–5 **(in Chinese with English abstract)**

Liu HB et al (2013) Determination of stable isotope composition in uranium geological samples. World Nucl Geosci 30:174–179

Liu Y, Hu K, Han SC, Sun ZZ (2015) The nature of ore-forming fluids of the Carlin-type gold deposit in southwest China: a case

from the Zimudang Gold Deposit. Resour Geol 65:136–159. https://doi.org/10.1111/rge.12060

Liu JZ et al (2017) New progress of exploration and research of Zhenfeng–Puan gold fully equipped exploration area. GuiZhou Geol 4:244–254 **(in Chinese with English abstract)**

Luo DW, Zeng GP (2018) Application and effects of singularity analysis in evaluating the denudation degree of Carlin-type gold deposits in southwest Guizhou, China. Ore Geol Rev 96:164–180

Murowchick JB, Barnes HL (1986) Marcasite precipitation from hydrothermal solutions. Geochim Cosmochim Acta 50:2615–2629. https://doi.org/10.1016/0016-7037(86)90214-0

Ohmoto H (1972) Systematics of sulfur and carbon isotopes in hydrothermal ore deposits. Econ Geol 67:551–578

Ohmoto H, Goldhaber MB (1997) Sulphides and carbon isotopes. In: Barnes HL (ed) Geochemistry of hydrothermal ore deposits, 3rd edn. Wiley, New York, pp 517–612

Pang BC, Lin CS, Luo XR, Hu CY, Zhuang XG (2005) The characteristic and origin of ore-forming fliud from micro-disseminated gold deposits in youjiang basin. Geol Prospect 1:13–17 **(in Chinese with English abstract)**

Peng YW, Gu XX, Zhang YM, Liu L, Wu CY, Chen SY (2014) Ore-forming process of the Huijiabao gold district, southwestern Guizhou Province, China: evidence from fluid inclusions and stable isotopes. J Asian Earth Sci 93:89–101. https://doi.org/10.1016/j.jseaes.2014.06.022

Potter RW, Clynne MA, Brown DL (1978) Freezing point depression of aqueous sodium chloride solutions. Econ Geol 73:284–285

Stenger DP, Kesler SE, Peltonen DR, Tapper CJ (1998) Deposition of gold in Carlin-type deposits: the role of sulfidation and decarbonation at Twin Creeks, Nevada. Econ Geol Bull Soc Econ Geol 93:201–215. https://doi.org/10.2113/gsecongeo.93.2.201

Su WC, Xia B, Zhang HT, Zhang XC, Hu RZ (2008) Visible gold in arsenian pyrite at the Shuiyindong Carlin-type gold deposit, Guizhou, China: implications for the environment and processes of ore formation. Ore Geol Rev 33:667–679. https://doi.org/10.1016/j.oregeorev.2007.10.002

Su WC, Heinrich CA, Pettke T, Zhang XC, Hu RZ, Xia B (2009) Sediment-Hosted gold deposits in Guizhou, China: products of wall-rock sulfidation by deep crustal fluids. Econ Geol 104:73–93. https://doi.org/10.2113/gsecongeo.104.1.73

Su WC, Zhang HT, Hu RZ, Ge X, Xia B, Chen YY, Zhu C (2012) Mineralogy and geochemistry of gold-bearing arsenian pyrite from the Shuiyindong Carlin-type gold deposit, Guizhou, China: implications for gold depositional processes. Miner Depos 47:653–662. https://doi.org/10.1007/s00126-011-0328-9

Su WC et al (2018) Carlin-type gold deposits in the Dian-Qian-Gui "Golden Triangle" of Southwest China. Rev Econ Geol 20:157–186

Tan QP, Xia Y, Xie ZJ, Yan J (2015a) Migration paths and precipitation mechanisms of ore-forming fluids at the Shuiyindong Carlin-type gold deposit, Guizhou, China. Ore Geol Rev 69:140–156. https://doi.org/10.1016/j.oregeorev.2015.02.006

Tan QP, Xia Y, Xie ZJ, Yan J, Wei DT (2015b) S, C, O, H, and Pb isotopic studies for the Shuiyindong Carlin-type gold deposit, Southwest Guizhou, China: constraints for ore genesis. Chin J Geochem 34:525–539

Tan LJ, Meng MH, Nie R, Li ST (2017a) Good prospecting potential for micro- and fine-grained disseminated gold deposits in Baogudi anticline area, Xingren County, Guizhou Province News Letters of China. Geol Surv 3:1–4

Tan QP, Yong X, Wang XQ, Zhuo JX, Wei DT (2017b) Carbon-oxygen isotopes and rare earth elements as an exploration vector for Carlin-type gold deposits: a case study of the Shuiyindong gold deposit, Guizhou Province, SW China. J Asian Earth Sci 148:1–12. https://doi.org/10.1016/j.jseaes.2017.08.013

Veizer J, Holser WT, Wilgus CK (1980) Correlation of $^{13}C/^{12}C$ and $^{34}S/^{32}S$ secular variation. Geochim Cosmochim Acta 44:579–588

Wang L, Zhang YW, Liu SG (2009) The application of regional gravity and magnetic data to delineaing intrusivie bodies and local geological structures in Guizhou Province. Geophys Geochem Explor 33:245–249 **(in Chinese with English abstract)**

Wang ZP, Xia Y, Song XY, Liu JZ, Yang CF, Yan BW (2013) Study on the evolution of ore-formation fluids for Au–Sb ore deposits and the mechanism of Au–Sb paragenesis and differentiation in the southwestern part of Guizhou Province, China. Chin J Geochem 32:56–68

Wang L, Long CL, Liu Y (2015) Discussion on concealed rock mass delineation and gold source in southwestern Guizhou. Geoscience 29:702–712 **(in Chinese with English abstract)**

Wei DT (2017) Study on the ore-forming source, the hydrothermal evolution and the ore-forming mechanism of the Nibao gold deposit, southwestern Guizhou Province, China. Dissertion, University of Chinese Academy of Sciences, p 152 **(in Chinese with English abstract)**

Wei DT, Xia Y, Tan QP, Xie ZJ, Yan J, Guo HY, Liu JZ (2016) Comparative study of the wallrock and ore and ore forming mechanisms at the Nibao gold deposit, Guizhou, China. Acta Petrol Sin 32:3343–3359 **(in Chinese with English abstract)**

Xia Y (2005) Characteristics and model for Shuiyindong gold deposit in southwestern Guizhou, China. PhD thesis, Institute of Geochemistry, Chinese Academy of Sciences, Guizhou, China, pp 69–75 **(in Chinese with English abstract)**

Xia Y, Zhang Y, Su WC, Tao Y, Zhang XC, Liu JZ, Deng YM (2010) Metallogenic model and prognosis of the Shuiyindong super-large stratabound Carlin-type gold deposit, southwestern Guizhou province, China. Acta Geol Sin 83:1473–1482 **(in Chinese with English abstract)**

Xie XY, Feng DS, Chen MH, Guo SX, Kuang SD, Chen HS (2016) Fluid inclusion and stable isotope geochemistry study of the Nibao gold deposit, Guizhou and insights into ore genesis. Acta Petrol Sin 32:3360–3376 **(in Chinese with English abstract)**

Xie ZJ, Xia Y, Cline JS, Yan BW, Wang ZP, Tan QP, Wei DT (2017) Comparison of the native antimony-bearing Paiting gold deposit, Guizhou Province, China, with Carlin-type gold deposits, Nevada, USA. Miner Depos 52:69–84. https://doi.org/10.1007/s00126-016-0647-y

Xie ZJ et al (2018) Magmatic origin for sediment-hosted Au deposits, Guizhou Province, China. In situ chemistry and sulfur isotope composition of pyrites, Shuiyindong and Jinfeng Deposits. Econ Geol 113:1627–1652. https://doi.org/10.5382/econgeo.2018.4607

Yan J, Hu RZ, Liu S, Lin YT, Zhang JC, Fu SL (2018) NanoSIMS element mapping and sulfur isotope analysis of Au-bearing pyrite from Lannigou Carlin-type Au deposit in SW China: new insights into the origin and evolution of Au-bearing fluids. Ore Geol Rev 92:29–41. https://doi.org/10.1016/j.oregeorev.2017.10.015

Yigit O, Hofstra AH (2003) Lithogeochemistry of Carlin-type gold mineralization in the Gold Bar district, Battle Mountain-Eureka trend, Nevada. Ore Geol Rev 22:201–224. https://doi.org/10.1016/s0169-1368(02)00142-7

Zhang XC, Spiro B, Halls C, Stanley CJ, Yang KY (2003) Sediment-hosted disseminated gold deposits in Southwest Guizhou, PRC: their geological setting and origin in relation to mineralogical, fluid inclusion, and stable-isotope characteristics. Int Geol Rev 45:407–470. https://doi.org/10.2747/0020-6814.45.5.407

Zhang Y, Xia Y, Su WC, Tao Y, Zhang XC, Liu JZ, Deng YM (2010) Metallogenic model and prognosis of the Shuiyindong super-large strata-bound Carlin-type gold deposit, southwestern Guizhou Province, China. Chin J Geochem 29:157–166

Zheng LL (2017) Mineralization mechanism and ore-forming process of the Nibao gold deposit in southwestern Guizhou, China. Dissertation, Guizhou University, p 141 (**in Chinese with English abstract**)

Zheng YF, Chen JF (2000) Stable isotope geochemistry. Science Press, Beijing, pp 36–274

Zhou YG, Liu JS, Wang ZH, Ouyang YF, Gao QZ, Liu DL, Huang YY (2009) The sources of ore-forming substance of Carlin-type gold deposit: a discussion based on the characteristics of regional stratigraphic geochemical evolution in "GoldTriangle" area of Yunnan, Guizhou, Guangxi Provinces. Guizhou Geol 16:199–208 **(in Chinese with English abstract)**

Zhu LM, Liu XF, Jin JF, He MY (1998) The study of the time-space distribution and source of ore-forming fluid for the fine-disseminated gold deposits in the Yunnan-Guizhou-Guangxi area. Sci Geol Sin 4:463–473 **(in Chinese with English abstract)**